XII. PLASMA ELECTRONICS*

Prof. L. D. Smullin	R. J. Briggs	L. M. Petrie, Jr.
Prof. H. A. Haus	J. R. Cogdell	W. D. Rummler
Prof. A. Bers	S. A. Evans	A. J. Schneider
Prof. W. D. Getty	E. T. Gerry	P. E. Serafim
Prof. D. J. Rose	B. A. Hartenbaum	P. S. Spangler
Prof. T. H. Dupree	H. Y. Hsieh	G. Theodoridis
Prof. L. M. Lidsky	G. I. Kachen	E. Thompson
Prof. E. P. Gyftopoulos	P. K. Karvellas	P. B. Ulrich
Dr. G. Fiocco	J. D. Levine	C. E. Wagner
D. S. Alles	L. N. Lontai	S. Wilensky
F. Alvarez de Toledo	D. L. Morse	H. L. Witting
W. L. Brassert	R. T. Nowak	J. C. Woo

A. BEAM-PLASMA DISCHARGES

1. SYSTEM A: MAGNETIC PROBE

Several magnetic probes have been constructed and used to aid in the diagnosis of the beam-plasma discharge (Fig. XII-1). The coils are 100 turns of No. 36 wire with an

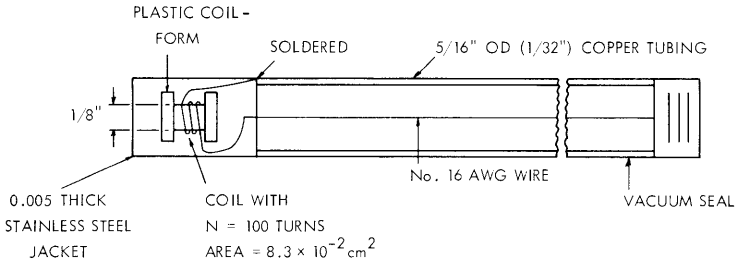

Fig. XII-1. Magnetic probe.

area of 8.3×10^{-2} cm^2. The coils are constructed with their axis either parallel or perpendicular to the axis of the coaxial line. The relationship between the voltage at the terminals and the changing magnetic field through the coil is expressed in Eq. 1.

$$V = NAg \frac{dB}{dt}, \tag{1}$$

where g is a frequency-dependent factor that accounts for the skin effect of the stainless-steel jacket. This factor is found experimentally by calibrating the probe in the field of a solenoid driven by a sinusoidal current source (Fig. XII-2). The effect of the jacket

*This work was supported in part by the National Science Foundation (Grant G-24073); in part by the U.S. Navy (Office of Naval Research) under Contract Nonr-1841(78); and in part by Purchase Order DDL B-00368 with Lincoln Laboratory, a center for research operated by Massachusetts Institute of Technology with the joint support of the U.S. Army, Navy, and Air Force under Air Force Contract AF 19(604)-7400.

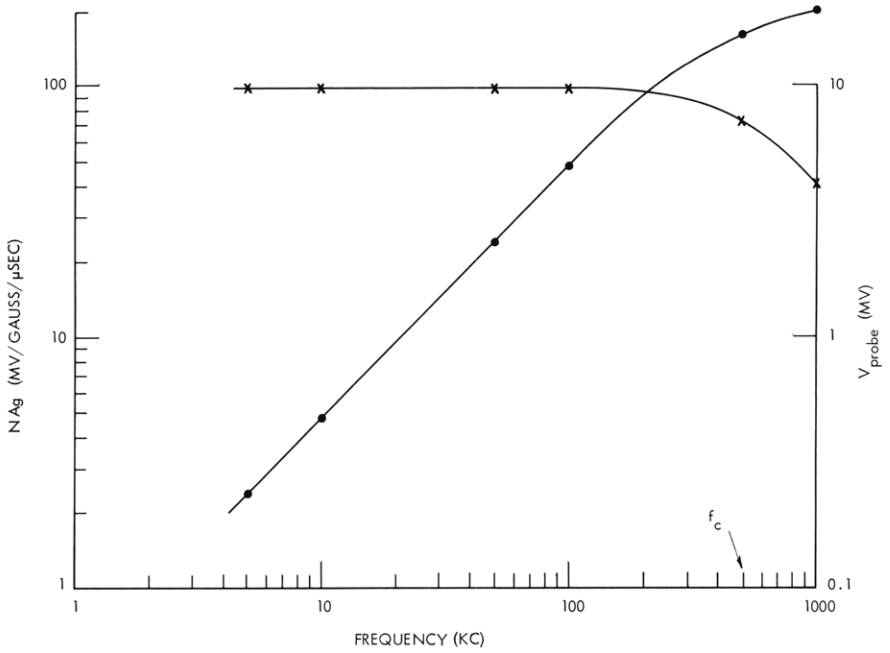

Fig. XII-2. Plot of V_{probe} vs frequency (...) and plot of NAg vs frequency (xxx) at constant current, 0.01 amp (1 amp = 7.8 gauss).

is to limit the high-frequency response of the coil. If the term dB/dt in Eq. 1 can be expressed as a series of impulse functions, the voltage response will be a series of scanning functions. To a good approximation, the width of the major lobe of the scanning function is equal to the inverse of the cutoff frequency defined in Fig. XII-2. If the impulse functions are far enough apart, the major lobes of the scanning functions will not overlap, and the area of the triangle circumscribed by the major lobe of the scanning function is equal to the area of the corresponding impulse.

Thus, in Fig. XII-3, we can relate the pulses in the magnetic probe voltage to step

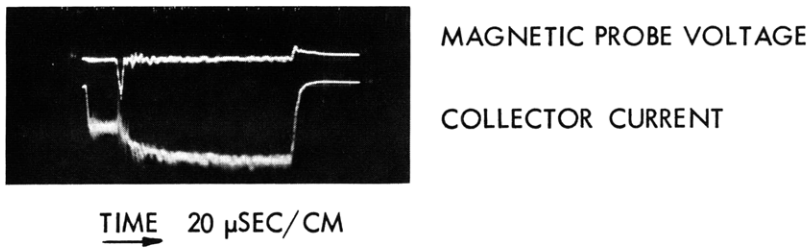

Fig. XII-3. Oscillogram of magnetic probe voltage and collector current. V_{beam} = 5 kv; pressure = 3×10^{-4} mm Hg hydrogen; B_o = 320 gauss. Calibration: I_{coll} = 0.2 amp/cm; V_{probe} = 5 mv/cm.

changes in the local axial field of the plasma (the coil axis was aligned parallel with the dc magnetic field). Typically, the changes in the local field are approximately 0.5 gauss. The first pulse occurs simultaneously with the break in beam current, and the second pulse, usually smaller but longer in duration, occurs at the end of the beam current (Fig. XII-3).

Figure XII-4b shows that by turning the probe 90° with respect to the dc magnetic field, the pulses disappear. At low pressures (5×10^{-6} mm Hg) when the electron beam does not initiate a beam-plasma discharge, there is no voltage induced on the magnetic

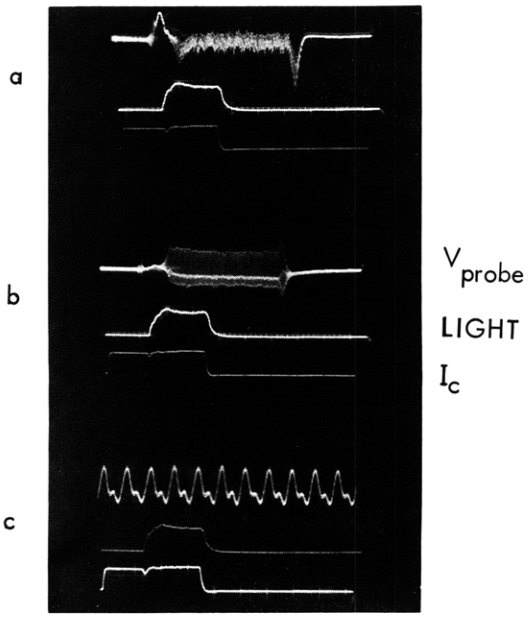

Fig. XII-4. Pulse structure and oscillatory nature of magnetic probe voltage. V_{beam} = 10 kv; pressure, 2.2×10^{-4} mm Hg hydrogen; B_o = 240 gauss.

(a) The magnetic probe is aligned with its coil axis parallel to the dc magnetic field.
Calibration: 20 μsec/cm and 10 mv/cm.

(b) The magnetic probe is aligned with its coil axis radially perpendicular to the dc magnetic field.
Calibration: 20 μsec/cm; 20 mv/cm.

(c) The magnetic probe voltage is expanded to 1 μsec/cm; 20 mv/cm.

In all three oscillograms, the light calibration is 50 μsec/cm; 5 volts/cm.
Collector current calibration: 50 μsec/cm; 0.5 amp/cm.

probe for any orientation of the probe axis. In Fig. XII-4a, the change in B_z measured from the pulse at the end of the beam-plasma discharge is 0.9 gauss.

Using the relationship

$$\frac{B\Delta B}{\mu_o} = e\Delta NT, \tag{2}$$

we obtain

$$\Delta NT = 5 \times 10^{24}\, B\Delta B. \tag{3}$$

If we assume a density of 10^{12}/cc, we can estimate an electron temperature of 11 ev.

In some experiments, it was observed that another set of pulses appears before the beam current ends (Fig. XII-5). This set of pulses can (tentatively) be interpreted as

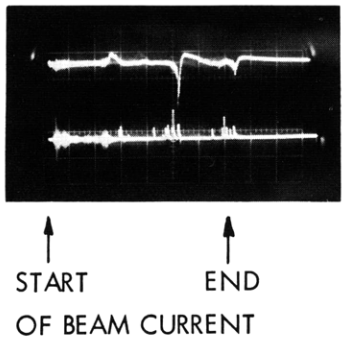

Figure XII-5.

"Collapse" and rebuild-up of beam-generated plasma. V_{beam} = 5 kv; pressure = 1.8×10^{-4} mm Hg hydrogen; B_o = 350 gauss. Calibration: time, 20 μsec/cm; V_{probe}, 5 mv/cm; x-ray, 50 mv/cm.

the "collapse" and rebuilding of the beam-generated plasma. On a simultaneous display of x-rays in Fig. XII-5, it is seen that the x-rays precede such a "collapse" of the

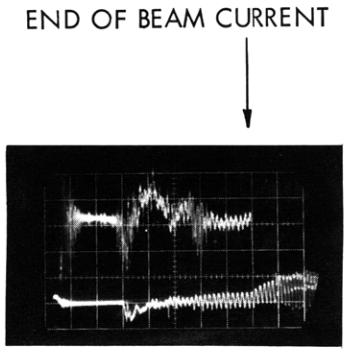

Figure XII-6.

Presence of 600-kc oscillation on collector current. V_{beam} = 10 kv; pressure = 2.2×10^{-4} mm Hg hydrogen; B_o = 340 gauss. Calibration: time, 10 μsec/cm; V_{probe} = 5 mv/cm; I_{coll}, 20 ma/cm.

plasma. This phenomenon has not been studied in great detail.

A very clean sinusoidal oscillation sometimes with second harmonics, with a frequency of 450 kc to 1 mc has also been observed (Figs. XII-4 and XII-6). This oscillation occurs at high beam voltages (~10 kv). The frequency of the oscillation gradually decreases as the magnetic field is increased by a factor of 3. The frequency of the oscillation does not depend on the mass of the gas (argon and hydrogen were used) or on

pressure. At high pressures (~1μ) the amplitude of the oscillation decreases. The oscillations start after the first pulse appears, and may last long after the beam current has ceased (Fig. XII-6). The oscillations are also seen on other collectors (Fig. XII-6).

These oscillations have a standing-wave character. The half wavelength of a 450-kc oscillation found from a movable magnetic probe is 15 cm. This gives a phase velocity of 1.35×10^7 cm/sec, which is larger than the acoustic velocity (~10^6 cm/sec) and smaller than the Alfvén velocity (~10^8 cm/sec). The mechanism of the generation of these oscillations is being studied.

H. Y. Hsieh

2. SYSTEM B: ROTATIONAL INSTABILITY AND QUENCHING

Studies of the beam-plasma discharge in the long solenoid apparatus (System B) have disclosed a low-frequency rotation of the plasma that is assumed to represent an instability or a mechanism by which the plasma leaks across the field. We have also observed

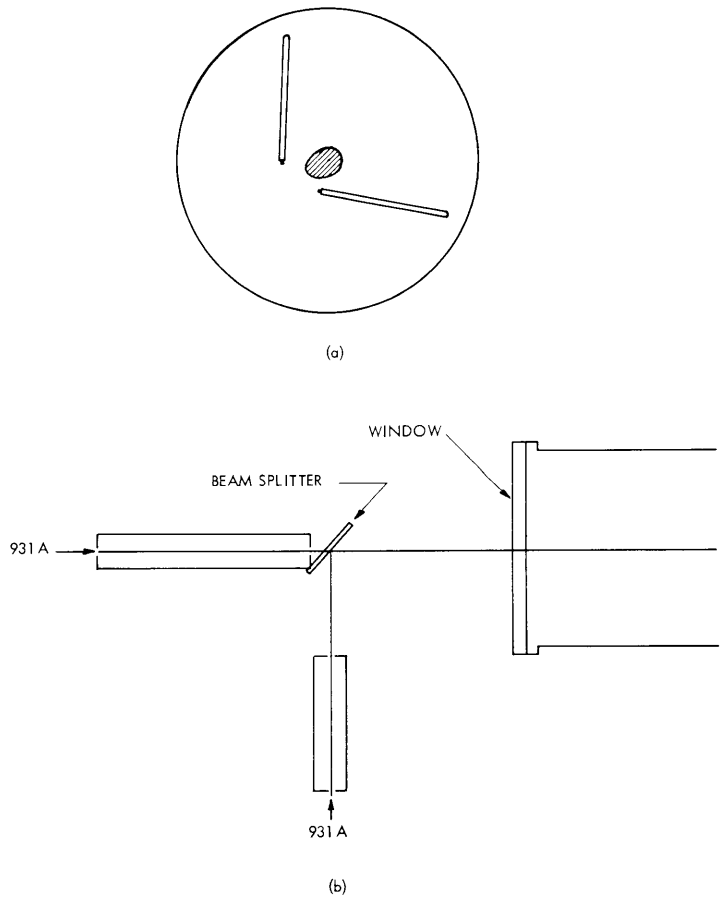

Fig. XII-7. (a) Plasma current probes.
(b) Space-time resolved light arrangement.

some critical values of magnetic field for which no beam-plasma interaction occurs.

a. Rotational Instability

Independent measurements of plasma currents and plasma light have been used to measure the rotation. The two experiments are illustrated in Fig. XII-7. Use of two small apertures for each photomultiplier and a beam splitter allowed simultaneous

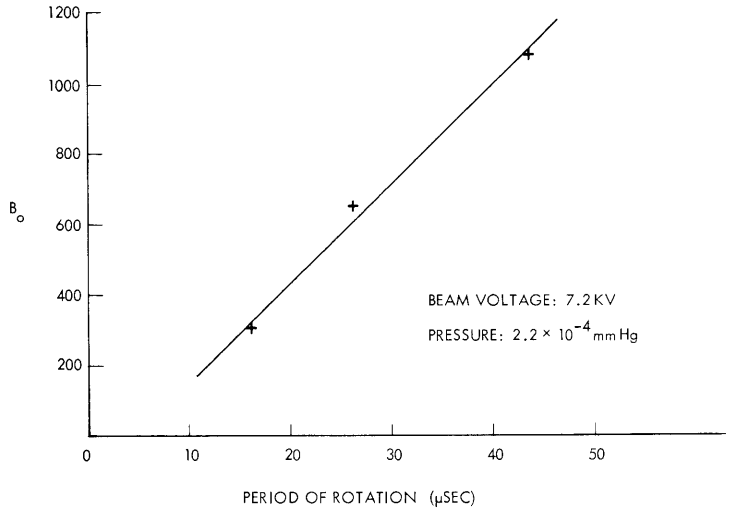

Fig. XII-8. Rotational period vs applied magnetic field.

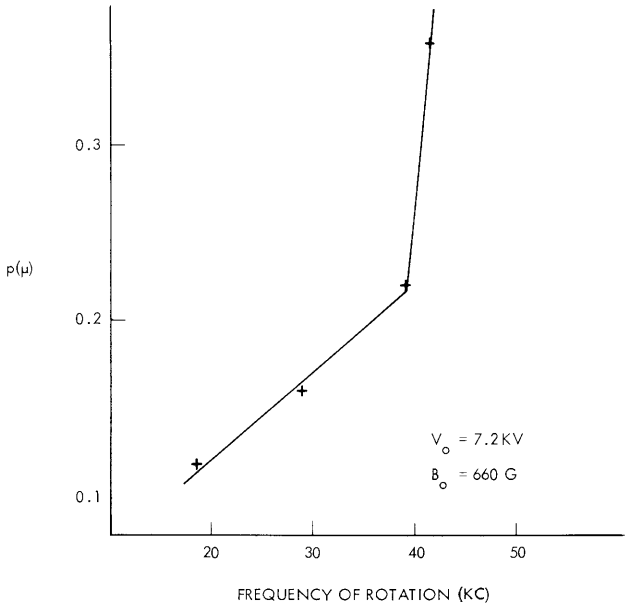

Fig. XII-9. Rotational frequency vs pressure.

measurements of light at difference positions in the cross section of the plasma column. The variation of rotational period with magnetic field (Fig. XII-8) suggests an E/B drift with $E \approx 2$ volts/cm. The variation of rotational frequency with gas pressure is shown in Fig. XII-9. Work is in progress to determine if a helical mode exists and to determine dc space-charge fields.

b. Quenching of Beam-Plasma Discharge

Values of the applied magnetic field for which the beam-plasma discharge is extinguished have been measured. For critical values of the magnetic field the beam passes through the gas without exciting microwave oscillations, although low-frequency oscillations (a few megacycles) are present.[1] The "stability" depends on pulse length.

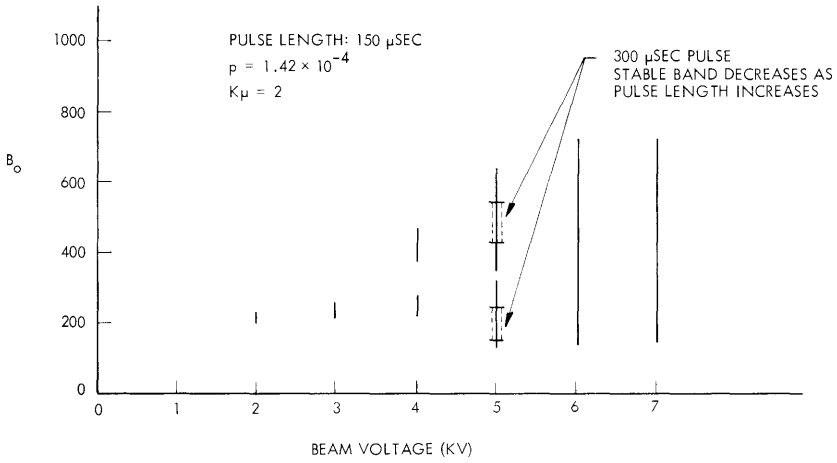

Fig. XII-10. Beam-gas stability. Solid line indicates band of stability.

Thus, a wide band of magnetic field strength produces stability for short pulses, but the range of B_o decreases as the pulse length increases. The stability depends on perveance and is more easily attained at lower pressures. The regions of stability at micro-perveance 2 are plotted in Fig. XII-10.

B. A. Hartenbaum

References

1. L. D. Smullin, W. D. Getty, B. A. Hartenbaum, and H. Y. Hsieh, Electron beam-plasma interaction experiments, Quarterly Progress Report No. 66, Research Laboratory of Electronics, M.I.T., July 15, 1962, pp. 116-123; see especially p. 123.

3. SYSTEM C: STRONG INTERACTION BETWEEN A HIGH-DENSITY, HOLLOW ELECTRON BEAM AND A PLASMA

For several years our experiments[1,2] on strong electron beam-plasma interactions have indicated that high beam perveance is important. Evidence of this can be seen by increasing the perveance by only 20-30 per cent. Such an increase usually results in stronger x radiation, rf oscillations, and light output from the plasma. There are good theoretical reasons for expecting this behavior. The one-dimensional theory[3] for collision- or temperature-limited reactive-medium amplification predicts that the maximum amplification rate increases rapidly with the ratio n_b/n_p, where n_b and n_p are the beam and plasma electron densities. Since the beam density is proportional to perveance for space-charge-limited flow, an increase in perveance would produce a greater amplification rate and consequently a stronger interaction. More recent theoretical work[4] has shown that a large value of n_b/n_p is important if low-frequency ion oscillations are to be excited. To investigate the interaction with a much denser beam than used heretofore, we have constructed an experiment in which the interaction between a high-perveance, hollow electron beam and a beam-generated plasma will be studied. In this report we shall describe the apparatus and some observations made in our first exploratory operation of the experiment.

The interaction takes place in a 6-inch diameter stainless-steel vacuum tube that is coaxial with a solenoid. The solenoid has an inside diameter of 7 inches, and outside

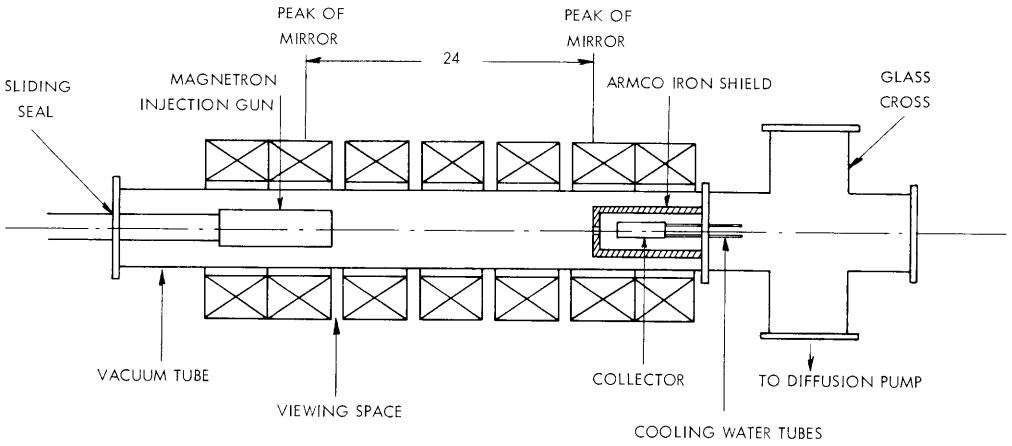

Fig. XII-11. Top view of hollow-beam experimental apparatus.

diameter of 13.5 inches, and is 40 inches long. The plasma can be observed through 1-inch diameter quartz windows that can be viewed through spaces between the coils of the solenoid. The vacuum chamber and solenoid are illustrated in Fig. XII-11.

The electron gun, which is also shown in Fig. XII-11, is mounted on a sliding tube that can be set at any desired axial position along the solenoid. All gun parts are nonmagnetic. An Armco iron shield is mounted at the opposite end of the vacuum tube. This shield produces a magnetic mirror and magnetically shields the electron-beam collector. A second magnetic mirror is produced near the electron gun by running higher currents through two of the solenoid coils. We thus have a magnetic bottle with a 2:1 mirror ratio at each end. The distance between the peaks of the field is 24 inches.

To obtain a dense electron beam, we are using the magnetron injection gun designed and deseribed by Poeltinger.[5] This gun is located at a peak of the mirror field. Its perveance ranges from 5×10^{-6} amp per $(\text{volt})^{3/2}$ to 20×10^{-6} amp per $(\text{volt})^{3/2}$, the range depending on the magnetic field and beam voltage. The outside diameter of the beam is approximately 0.5 inch, and the beam thickness is less than 10 per cent of its diameter. The electron density is 10^{11} electrons/cm^3.

An artificial-delay-line pulser has been built to drive the electron gun. This system is designed to operate up to 20 kv and 30 amps at a repetition rate of 10 pps. The pulse length is 300 μsec. A pulse transformer is used to match the 30-ohm line to the electron gun, whose nominal impedance is 500 ohms.

In the experiment the hollow beam is injected into the magnetic bottle near the peak of one of the mirrors. The beam diameter increases as it passes into the region of lower field between the mirrors. At the beam energies used in the experiment the beam passes through the second mirror and into the shielded collector, which is shown in Fig. XII-11. With the hydrogen pressure set in the range 10^{-4}-10^{-3} mm Hg in the vacuum tube, a plasma is rapidly generated by the beam. We have observed that this plasma strongly interacts with the hollow beam.

Our first exploratory experiments were made at beam voltages and currents up to 10 kv and 10 amps. The electron gun operated well in this range, and strong interaction was observed. Each beam pulse produced a very bright plasma whose color was light blue or light pink. At some operating conditions it was found that the light output was delayed 100-200 μsec after the start of the beam pulse. During this period, the current to the vacuum-tube walls was carried by ions and oscillated violently from zero to several amperes at frequencies of approximately 10 mc. Similar behavior has been observed previously.[2] A scintillator showed that x radiation escaped from the vacuum tube. Measurements with aluminum absorbers indicated that the x-ray energy, which was assumed to be monoenergetic, was in the range 17-20 kv. Observations of the microwave spectrum of the energy radiated by the plasma were made with the gun operating at 9 kv and 7.5 amps, and with the hydrogen pressure at 0.3 μ Hg. Strong microwave output was observed at frequencies as high as 32 kmc. The maximum oscillation frequency is assumed to equal the plasma frequency.[1] Strong oscillations were also observed at lower frequencies, particularly in the range 100-1500 mc. Plasma

oscillations at a plasma frequency of 32 kmc would correspond to a density of 10^{13} electrons/cm^3. The neutral gas density at the pressure of 0.3 μ Hg has approximately the same value, and therefore the plasma may be fully ionized.

W. D. Getty, L. D. Smullin

References

1. L. D. Smullin and W. D. Getty, Generation of a hot, dense plasma by a collective beam-plasma interaction, Phys. Rev. Letters 9, 3-6 (1962).

2. L. D. Smullin, B. A. Hartenbaum, and H. Y. Hsieh, Electron beam-plasma interaction experiments, Quarterly Progress Report No. 67, Research Laboratory of Electronics, M.I.T., October 15, 1962, pp. 71-76.

3. G. D. Boyd, L. M. Field, and R. W. Gould, Excitation of plasma oscillations and growing plasma waves, Phys. Rev. 109, 1393 (1958).

4. R. J. Briggs and A. Bers, Electron-beam interactions with ions in a warm plasma, Quarterly Progress Report No. 69, Research Laboratory of Electronics, M.I.T., April 15, 1963, pp. 65-74.

5. A. Poeltinger, High-perveance hollow electron-beam study, Quarterly Progress Report No. 66, Research Laboratory of Electronics, M.I.T., July 15, 1962, pp. 25-29.

4. FAST-ACTING, CURRENT-ACTUATED GAS VALVE

The purpose of this investigation was to develop a valve that would admit repeatable quantities of gas (0.1-1 cc at S.T.P.) into a vacuum in pulses of less than 100 μsec. The valve that was developed is discussed in a Master's thesis[1]; therefore, only a brief discussion of its operation and characteristics will be given here.

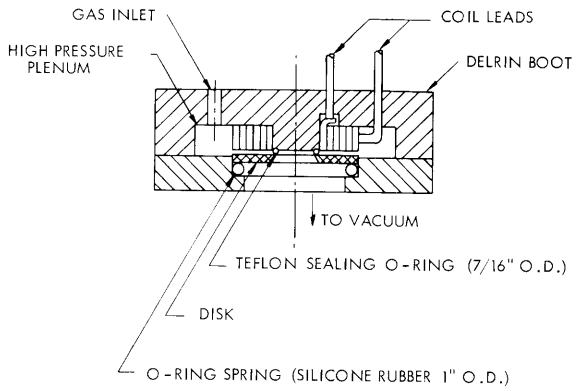

Fig. XII-12. Magnetically driven gas valve.

The valve shown in Fig. XII-12 consists of a 1-inch O.D. disk of copper, brass or aluminum which is held against the Teflon O-ring by the precompressed silicone rubber

O-ring. The 1-inch O.D. coil (1.7 μh) consists of nine turns of 0.25 × 0.021-inch copper tape, insulated with 0.004 Mylar ribbon and potted in epoxy. The 0.25-inch diameter coil leads are connected through a mechanical switch to a 2-μf capacitor that is initially charged to 3500-7000 volts. The ringing frequency of this circuit is approximately 90 kc, and its damping time constant varies between 4 μsec and 10 μsec, the variation depending on the material of the disk.

When the capacitor is discharged through the coil, the eddy currents induced in the disk cause a repulsive force between the coil and the disk. This force causes the disk to move downward and thus allows the gas to pass between the disk and Teflon O-ring, and then through the central hole in the disk. The energy-conversion efficiency of this device is approximately 0.5 per cent; however, the available force may be as high as 700-1000 pounds for a period of a few microseconds.

The period and amplitude of the disk motion may be accurately calculated by considering the valve as a damped spring-mass system in which the spring is precompressed and restrained from moving through its equilibrium position. The damping ratio is approximately $\rho = 0.88$ (in this case the damping is due to hysteresis in the O-ring spring). The period of the motion is not affected by variations in the initial capacitor voltage. However, when positive stops are added in order to limit the motion of the disk, the period varies not only with the stiffness and precompression of the O-ring but also with the initial capacitor voltage (the period decreases with increasing voltage) and the allowable excursion of the disk. In practice, the period could be varied 50-250 μsec, and the maximum amplitude was approximately 0.025 inch.

Finally, there are several difficulties that still must be corrected. The first is that the disk bounces on the Teflon O-ring, thereby reopening the valve. This bouncing is especially pronounced when high initial capacitor voltages are used with low precompression of the O-ring spring. This may be rectified by using a softer sealing O-ring. A second difficulty, excessive heating of the coil and disk, may be encountered if the valve is to be cycled rapidly for long periods of time.

D. S. Alles, L. D. Smullin

References

1. D. S. Alles, Design and Development of a Fast-Acting Valve for Plasma Research, S.M. Thesis, Department of Mechanical Engineering, M.I.T., May 1963.

B. INSTABILITY IN THE HOLLOW-CATHODE DISCHARGE

As previously reported,[1] a rotating instability has been observed in the hollow-cathode discharge. The instability causes a cloud of plasma, a "spoke," to rotate about the axis of the system, for sufficiently large values of axial magnetic field. This spoke

has fairly uniform properties in the direction of the magnetic field, and exhibits no helical pattern. During the past quarter, time-resolved, space-potential measurements have been made, and a theoretical study has been initiated to describe macroscopic, low-frequency instabilities of a magnetized plasma.

1. Effect of the Instability on Diffusion

Measurements of the average density at a point 4 inches from the system axis vs magnetic field indicate that the presence of the instability is a major factor in the dif-

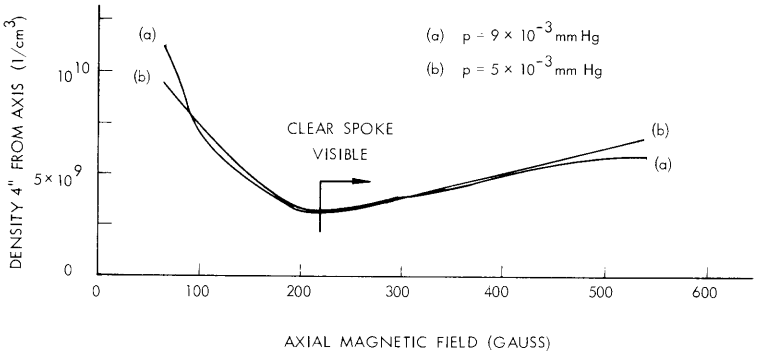

Fig. XII-13. Density 4 inches from system axis vs magnetic field. Clear spoke is visible above ~220 gauss.

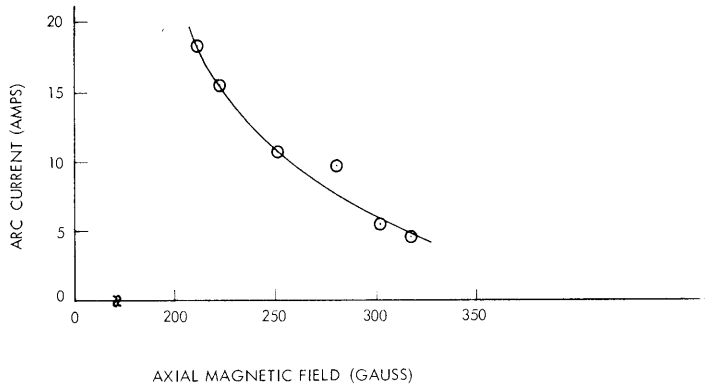

Fig. XII-14. Minimum axial magnetic field for instability vs arc current.

fusion of plasma across the magnetic field (Fig. XII-13). The average density increases with increasing magnetic field after the instability appears. Plasma density in the source region remains nearly constant as the magnetic field is varied.

2. Onset of the Instability

As the arc current is increased, the spoke appears at decreasing values of magnetic field (Fig. XII-14). To investigate this effect, the space-potential distribution was measured for various values of arc current and magnetic field (Fig. XII-15). The spoke appears when the space potential rises to approximately 10 volts with respect to the walls, and decreases for increasing radius. It is observed that the spoke rotates about the field lines in the left-handed sense, which is the direction of the Hall drift for an outward-directed electric field. The spoke is present only in the region in which the electric field is directed outward. The inner boundary of this region moves closer to the axis as the magnetic field is increased.

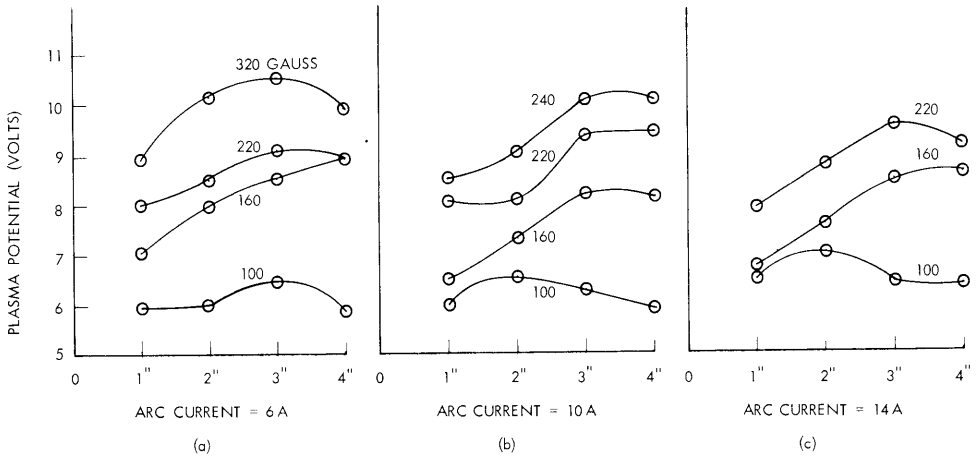

Fig. XII-15. Plasma-potential distribution for various magnetic fields and arc currents. Top curve indicates distribution as instability appears.

3. Time-Resolved Space-Potential Measurements

To correlate the motion of the spoke and particles within the spoke with theory, a knowledge of the density and potential gradients is necessary. The density measurements have been previously reported, [1] and space-potential measurements have now been completed.

Figure XII-16 shows the variation of space potential with time for various radial positions. Since the spoke moves approximately as a rigid body, this is equivalent to plotting the potential around the circumference of a circle centered on the system's axis. The bottom curve is proportional to plasma density at a distance of 3 inches from the system axis. It shows the slowly rising leading edge and the sharply dropping trailing edge of the distrubance.

If the space potential within the spoke is plotted against radius, a linear descent with radius is obtained. This explains our observation that the spoke is clearest when the magnetic field is shaped so that its axial component falls off approximately as 1/r to give an approximately constant value of E/rB. The rotational frequency calculated from the Hall mobility agrees with the observed behavior by better than a factor of 2, over a range of magnetic field from 300 gauss to 500 gauss.

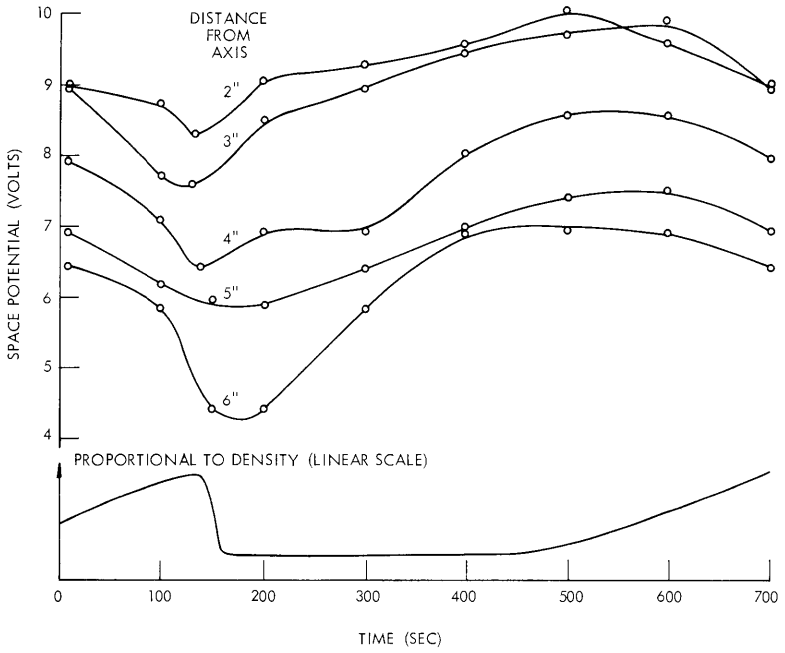

Fig. XII-16. Space potential vs time. Period of rotation, 600 μsec. Density 3 inches from axis plotted for reference. Azimuthal E-field to the right corresponds to outward radial Hall drift.

When the space potential in Fig. XII-16 descends to the right at a given radius, the result is an azimuthal electric field that drives particles radially outward at a speed determined by the Hall mobility. These phenomena occur in the region of increasing density. The Hall mobility tends to force particles inward after the spoke has passed, possibly explaining its sharp trailing edge. The net flux of particles will be outward, however, since the region of inward flow is one of very low density.

In comparing the radial flux of particles caused by the instability with the unperturbed flux, we note that the radial and azimuthal electric fields are roughly the same size, but the Hall mobility is much larger than the perpendicular mobility. With this kind of reasoning, the particle flux can be conservatively estimated to be a factor of 10 larger than the unperturbed flux.

D. L. Morse

References

1. D. L. Morse, Instability in the hollow-cathode discharge, Quarterly Progress Report No. 69, Research Laboratory of Electronics, M.I.T., April 15, 1963, p. 54.

C. INTERACTION BETWEEN AN ELECTRON BEAM AND PLASMAS

1. Model Description

The plasma consists of electrons neutralized by ions of finite mass. Their unperturbed charge density may have a transverse variation. The dc charge density and the well-defined velocity along the axis of the waveguide of the electrons in the beam also may have a transverse variation. The electrons in the beam also are neutralized by ions of finite mass.

The waveguide is a hollow, uniform, metal tube of arbitrary cross section. Therefore we shall use a system of generalized orthogonal coordinates with the z axis taken to be parallel to the axis of the waveguide. There is a uniform, finite, axial magnetostatic field along the axis of the waveguide.

The treatment is relativistic and non quasi-static and makes use of the small-signal theory. We neglect temperature and pressure gradients, as well as collisions.

In our previous report[1] we derived the dielectric tensor, which proved to be non-Hermitian because we neglected the term $\bar{v}_o \times \bar{B}$ in the Lorentz force equation. We are not permitted to omit this term, even for a nonrelativistic treatment. The consideration of the $\bar{v}_o \times \bar{B}$ term will make the dielectric tensor Hermitian, as it must be for a lossless passive system.

2. Dielectric Tensor

From the Lorentz force equation, we find

$$\bar{v}_m = j\bar{\bar{M}}_m(\bar{E} + \bar{v}_{om} \times \bar{B}) + j\bar{i}_z \frac{\bar{v}_{mT} \cdot \nabla_T v_{mo}}{\omega_{rm}} . \tag{1}$$

The subscript m denotes the species of particle and can be e for plasma electrons, i for ions, and b for beam electrons.

The tensor $\bar{\bar{M}}_m$ has the form:

$$\bar{\bar{M}}_m = \begin{bmatrix} M_{\perp m} & -jM_{xm} & 0 \\ jM_{xm} & M_{\perp m} & 0 \\ 0 & 0 & M_{\parallel m} \end{bmatrix} . \tag{2}$$

Let $R_{om} = [1-(v_{om}^2/c^2)]^{-1/2}$; $\eta_m = e_m/m_{om}$; $\omega_{cm} = (\eta_m/R_{om})\, B_o$, and $\omega_{rm} = \omega + j\gamma\nu_{om}$. Then the elements of the mobility tensor are

$$M_{\perp m} = \frac{\eta_m}{R_{om}} \frac{\omega_{rm}}{\left(\omega_{cm}^2-\omega_{rm}^2\right)} \tag{3a}$$

$$M_{xm} = \frac{\eta_m}{R_{om}} \frac{\omega_{cm}}{\left(\omega_{cm}^2-\omega_{rm}^2\right)} \tag{3b}$$

$$M_{\parallel m} = -\frac{\eta_m}{R_{om}^3} \frac{1}{\omega_{rm}}. \tag{3c}$$

By using the following relation from Maxwell's equations:

$$B_T = j\frac{(\nabla\times\bar{E})_T}{\omega} = -j\frac{\bar{i}_z\times[\nabla_T E_z+\gamma\bar{E}_T]}{\omega}, \tag{4}$$

Eq. 1 may be written

$$\bar{v}_m = j\bar{\bar{M}}_{o\beta m}\bar{E}. \tag{5}$$

Here,

$$\bar{\bar{M}}_{op,m} = \bar{\bar{M}}_m \left[\begin{array}{c:c} \frac{\omega_{rm}}{\omega}\bar{\bar{I}}_T & j\frac{\nu_{om}}{\omega}\nabla_T \\ \hdashline 0 & 1 \end{array}\right], \tag{6}$$

and $\bar{\bar{I}}_T$ is the 2×2 identity matrix.

The dielectric tensor $\bar{\bar{K}}_{op}$ is defined by the equation

$$\bar{\bar{K}}_{op}\cdot\bar{E} = \bar{E} + \frac{\bar{J}}{j\omega\epsilon_o}. \tag{7}$$

By using the definition of current densities, the law of conservation of charges (Eqs. 1 and 7), we obtain

$$\bar{\bar{K}}_{op} = \bar{\bar{I}} + \frac{1}{\epsilon_o\omega}\sum_m \left[\begin{array}{c:c} \rho_{om}\bar{\bar{I}}_T & 0 \\ \hdashline j\nabla_T\frac{\rho_{om}v_{om}}{\omega_{rm}} & \frac{\rho_{om}}{\omega_{rm}} \end{array}\right] \bar{\bar{M}}_{op,m}, \tag{8}$$

with the explicit form

$$\bar{\bar{K}}_{op} = \left[\begin{array}{cc:c} K_\perp & -jK_x & j\frac{K_4}{k_o}\nabla_T - \frac{K_5}{k_o}\bar{i}_z \times \nabla_T \\ jK_x & K_\perp & \\ \hdashline j\nabla_T \cdot \frac{K_4}{k_o}\bar{i}_z + \bar{i}_z \cdot \nabla_T \times \frac{K_5}{k_o} & & K_{||} - \nabla_T \cdot \frac{K_6}{k_o^2}\nabla_T + j\bar{i}_z \cdot \nabla_T \times \frac{K_7}{k_o^2}\nabla_T \end{array}\right] . \tag{9}$$

It should be noted that in the tensor of Eq. 9, which determines the electric displacement vector $\bar{D} = \bar{\bar{K}} \cdot \bar{E}$, the upper right operator is a 1×2 matrix operating on E_z, and the lower left operator is a 2×1 matrix operating on the transverse components of $\bar{E}$; the lower right operator is a 1×1 matrix operating on only E_z.

Let

$$\omega_{pmT}^2 = \frac{\eta_m}{R_{om}}\frac{\rho_{om}}{\epsilon_o} = \frac{\rho_{om} e_m}{\epsilon_o m_{mT}}$$

and

$$\omega_{pmz}^2 = \frac{\eta_m}{R_{om}^3}\frac{\rho_{om}}{\epsilon_o} = \frac{\rho_{om} e_m}{\epsilon_o m_{mz}}.$$

Then the elements of the $\bar{\bar{K}}_{op}$ tensor are given by

$$K_\perp = 1 + \frac{1}{\omega^2}\sum_m \frac{\omega_{pmT}^2 \omega_{rm}^2}{\omega_{cm}^2 - \omega_{rm}^2} \tag{10a}$$

$$K_x = \frac{1}{\omega^2}\sum_m \frac{\omega_{pmT}^2 \omega_{cm} \omega_{rm}}{\omega_{cm}^2 - \omega_{rm}^2} \tag{10b}$$

$$K_{||} = 1 - \sum_m \frac{\omega_{pmz}^2}{\omega_{rm}^2} \tag{10c}$$

$$\frac{K_4}{k_o} = \frac{1}{\omega^2}\sum_m \frac{\omega_{pmT}^2 \omega_{rm}}{\omega_{cm}^2 - \omega_{rm}^2} v_{om} \tag{10d}$$

$$\frac{K_5}{k_o} = \frac{1}{\omega^2} \sum_m \frac{\omega_{pmT}^2 \omega_{cm}}{\omega_{cm}^2 - \omega_{rm}^2} v_{om} \tag{10e}$$

$$\frac{K_6}{k_o^2} = \frac{1}{\omega^2} \sum_m \frac{\omega_p^2 \omega_{pmT}^2}{\omega_{cm}^2 - \omega_{rm}^2} v_{om}^2 \tag{10f}$$

$$\frac{K_7}{k_o^2} = \frac{1}{\omega^2} \sum_m \frac{\omega_{pmT}^2 \omega_{cm}}{\omega_{rm}\left(\omega_{cm}^2 - \omega_{rm}^2\right)} v_{om}^2 \tag{10g}$$

3. Hermitian Character of the $\overline{\overline{K}}_{op}$ Tensor

In the following discussion we shall write $\overline{\overline{K}}_{op}$ as $\overline{\overline{K}}$. For propagating wave, $\gamma = j\beta$, in a lossless passive system we can show[2] that

$$\int_A \overline{E}_2^* \cdot \overline{\overline{K}}_h \cdot \overline{E}_1 \, da - \int_A \overline{E}_1 \cdot \overline{\overline{K}}_h^* \cdot \overline{E}_2^* \, da = 0. \tag{11}$$

Relation (11) applied for $\overline{E}_1 = \overline{E}_2 = \overline{E}$ shows that $\int_A \overline{E}^* \cdot \overline{\overline{K}} \cdot \overline{E} \, da$ is a real number. We may easily see

$$\frac{1}{2}\nabla \cdot (\overline{E} \times \overline{H}^*) = -j2\omega\left(\frac{1}{4}\mu_o |\overline{H}|^2 - \frac{1}{4}\epsilon_o \overline{E}^* \cdot \overline{\overline{K}} \cdot \overline{E}\right) \tag{12}$$

that for a lossless passive system Re $\int_A \frac{1}{2} (\overline{E}_T \times \overline{H}_T^*) \cdot \overline{i}_z \, da = 0$. The integral $\int_A \overline{E}^* \cdot \overline{\overline{K}} \cdot \overline{E} \, da$ must be a real number.

In general, $\gamma = \alpha + j\beta$. In this case, the $\overline{\overline{K}}$ tensor has Hermitian and anti-Hermitian parts: $\overline{\overline{K}} = \overline{\overline{K}}_h + \overline{\overline{K}}_a$. The definition for $\overline{\overline{K}}_a$ is

$$\int \overline{E}_2^* \cdot \overline{\overline{K}}_a \cdot \overline{E}_1 \, da + \int \overline{E}_1 \cdot \overline{\overline{K}}_a^* \cdot \overline{E}_2^* \, da = 0. \tag{13}$$

In the above-given proof for the Hermitian character of $\overline{\overline{K}}$ for $\gamma = j\beta$, we have used the property that the K's in Eqs. 10 are real for $\gamma = j\beta$. Therefore for $\gamma = \alpha + j\beta$ the $\overline{\overline{K}}_h$ will be found when we consider the real part of the K's, and the $\overline{\overline{K}}_a$, when we consider the imaginary part of the K's.

There are many applications of Eq. 12. One of them is the extension of the variational principle for the propagation constant γ to the beam-plasma system.[2]

4. Plane Waves

If we assume a plane wave of the form $\exp(j\omega t - j\overline{k} \cdot \overline{r})$ with $\overline{k}$ on the x-z plane, the dielectric tensor, Eq. 9, becomes

$$K = \begin{bmatrix} K_\perp & -jK_x & +K_4\frac{k_x}{k_o} \\ jK_x & K_\perp & jK_5\frac{k_x}{k_o} \\ K^4\frac{k_x}{k_o} & -jK_5\frac{k_x}{k_o} & K_{||} + K_6\frac{k_x^2}{k_o^2} \end{bmatrix}. \tag{14}$$

This relation has already been used for the investigation of various waves.[3]

5. Field Analysis

We shall assume hereafter uniform dc charge density and dc beam velocity. The longitudinal fields are coupled, as in the case of plasma alone[4,5]:

$$\nabla_T^2 E_z + aE_z = bH_z \tag{15}$$

$$\nabla_T^2 H_z + cH_z = dE_z. \tag{16}$$

The coefficients now are

$$a = \frac{K_{||}\left(K_\perp k_o^2 + \gamma^2\right)}{K_\perp - j\frac{2\gamma K_4}{k_o} - \frac{\gamma^2 K_6}{k_o^2} + K_4^2 - K_\perp K_6} \tag{17a}$$

$$b = j\omega\mu_o \frac{j\gamma\left(K_x - \frac{j\gamma K_5}{k_o}\right) + k_o(K_\perp K_5 - K_x K_4)}{K_\perp - j\frac{2\gamma K_4}{k_o} - \frac{\gamma^2 K_6}{k_o^2} + K_4^2 - K_\perp K_6} \tag{17b}$$

$$c = \gamma^2 + k_o^2 K_\perp - k_o^2 K_x^2 \frac{\left(1 - \frac{j\gamma}{k_o}\frac{K_5}{K_x}\right)^2 - K_\perp\frac{K_5^2}{K_x^2} - K_6 + 2\frac{K_4 K_5}{K_x}}{K_\perp - j\frac{2\gamma K_4}{k_o} - \frac{\gamma^2 K_6}{k_o^2} + K_4^2 - K_\perp K_6} \tag{17c}$$

$$d = -\frac{\epsilon_o}{\mu_o} K_{||} b. \tag{17d}$$

The transverse fields are given in terms of the longitudinal fields by the relations

$$\begin{bmatrix} E_T \\ \bar{H}_T \\ i_z \times \bar{E}_T \\ i_z \times \bar{H}_T \end{bmatrix} = \begin{bmatrix} P & r & Q & s \\ T & p & U & q \\ -Q & -s & P & s \\ -U & -q & T & p \end{bmatrix} \begin{bmatrix} \nabla_T E_z \\ \nabla_T H_z \\ i_z \times \nabla_T E_z \\ i_z \times \nabla_T H_z \end{bmatrix}. \tag{18}$$

Here,

$$P = p - \omega\epsilon_o \frac{K_4}{k_o} s - j\omega\epsilon_o \frac{K_5}{k_o} r \tag{19a}$$

$$Q = q + \omega\epsilon_o \frac{K_4}{k_o} r - j\omega\epsilon_o \frac{K_5}{k_o} s \tag{19b}$$

$$T = t - \omega\epsilon_o \frac{K_4}{k_o} q - j\omega\epsilon_o \frac{K_5}{k_o} p \tag{19c}$$

$$U = u + \omega\epsilon_o \frac{K_4}{k_o} p - j\omega\epsilon_o \frac{K_5}{k_o} q, \tag{19d}$$

and p, q, r, s, t, and u are the known expressions.[5]

Our formulation for the beam-plasma system is similar to the formulation for plasma alone. Hence, for the rest of this report, we can use techniques and results that are already known.[4, 6]

The dispersion relation is

$$p^4 - (a+c)p^2 + ac - bd = 0. \tag{20}$$

The determinantal equation is derived from boundary conditions. For a completely filled circular waveguide it has the same form as for an anisotropic plasma.

$$A_1 \frac{J_n'(p_1 r_o)}{J_n(p_1 r_o)} - A_2 \frac{J_n'(p_2 r_o)}{J_n(p_2 r_o)} = jnA_3, \tag{21}$$

where A_1, A_2, and A_3 are algebraic functions of ω, γ, ν_{om}, ω_{pm}, ω_{cm}, p_1, and p_2.

6. Energy-Power Theorems and Variation Theorems

Assuming that the fields are of the form $\bar{A}(u_1, u_2, z, t) = \bar{A}(u_1, u_2) \exp(j\omega t - \gamma z)$ and manipulating Maxwell's equations, we obtain

$$\alpha P_e = -\omega \operatorname{Im} U_{\epsilon a} \tag{22}$$

$$\alpha Q_e = \omega(U_m - U_{\epsilon h}) \tag{23}$$

$$\beta P_e = \omega(U_{mT} - U_{mz} + U_{\epsilon Th} - U_{\epsilon zh} + 2 \operatorname{Re} U_{\epsilon zTa}) \tag{24}$$

$$\beta Q_e = \omega \operatorname{Im} (U_{\epsilon za} - U_{\epsilon Ta} - 2U_{\epsilon zTh}), \tag{25}$$

where

$$P_e + jQ_e = \int_A \frac{1}{2} \bar{E}_T \times \bar{\bar{H}}_T^* \cdot \bar{i}_z \, da \tag{26a}$$

$$U_\epsilon = \int \frac{1}{4} \epsilon_o \bar{E}^* \cdot \bar{\bar{K}} \cdot \bar{E} \, da \tag{26b}$$

$$U_{\epsilon T} = \int \frac{1}{4} \epsilon_o \bar{E}_T^* \cdot \bar{\bar{K}}_T \cdot \bar{E}_T \, da \tag{26c}$$

$$U_{\epsilon z} = \int \frac{1}{4} \epsilon_o E_z^* K_z E_z \, da \tag{26d}$$

$$U_{\epsilon zT} = \int \frac{1}{4} \epsilon_o \bar{E}_T^* \cdot \bar{\bar{K}}_{Tz} E_z \, da \tag{26e}$$

$$U_m = \int \frac{1}{4} \mu_o |\bar{H}|^2 \, da. \tag{26f}$$

The subscript h (or a) means that we must consider the Hermitian (or anti-Hermitian) part of $\bar{\bar{K}}$ in the corresponding formulae.

By use of Maxwell's equations and their variations, we get

$$\delta(\alpha P_e) = -\delta(\omega \operatorname{Im} U_{\epsilon a}) \tag{27}$$

$$\begin{aligned}
\delta \alpha Q_e = &-\frac{P}{2} \operatorname{Re} \int (\delta \bar{E}_T \times \bar{H}_T^* - \bar{E}_T \times \delta \bar{H}_T^*) \cdot \bar{i}_z \, da \\
&+ \delta\omega(U_{mT} - U_{mz}) + \int \left[\frac{1}{4} \epsilon_o E_z^* \delta(\omega K_{zh}) E_z - \frac{1}{4} \epsilon_o \bar{E}_T^* \cdot \delta(\omega \bar{\bar{K}}_{Th}) \cdot \bar{E}_T\right] da \\
&- \frac{\omega \epsilon_o}{2} \operatorname{Re} \int [\delta E_Z^* (\bar{\bar{K}}_{zTh} \cdot \bar{E}_T + K_{za} E_z) - \delta \bar{E}_T^* \cdot (\bar{\bar{K}}_{Tzh} \cdot E_z + \bar{\bar{K}}_{Ta} \cdot \bar{E}_T)] \, da \\
&- \frac{\epsilon_o}{2} \operatorname{Re} \int \bar{E}_T^* \cdot \delta(\omega \bar{\bar{K}}_{aTz}) E_z \, da
\end{aligned} \tag{28}$$

$$\delta\beta P_e = -\frac{a}{2}\,\mathrm{Im}\int (\delta\bar{E}_T \times \bar{\bar{H}}_T^* - \bar{E}_T \times \overline{\delta H}_T^*)\cdot i_z\,da + U_m\delta\omega$$

$$+\int \frac{1}{4}\epsilon_o \bar{E}^*\cdot\delta(\omega\bar{\bar{K}}_h)\cdot\bar{E}\,da - \frac{\omega\epsilon_o}{2}\,\mathrm{Re}\int \delta\bar{E}^*\cdot\bar{\bar{K}}_a\cdot\bar{E}\,da \tag{29}$$

$$\delta(\beta Q_e) = \delta\left[\omega\,\mathrm{Im}\,(U_{\epsilon za} - U_{\epsilon TQ} - 2U_{\epsilon z Th})\right] \tag{30}$$

If $a = 0$ ($\bar{\bar{K}} = \bar{\bar{K}}_h$), Eq. 29 gives

$$\frac{\partial\omega}{\partial\beta} = \frac{P_e - \int \frac{1}{4}\epsilon_o \bar{E}^*\cdot\frac{\partial(\omega\bar{\bar{K}})}{\partial\beta}\cdot\bar{E}\,da}{\int\left[\frac{1}{4}\mu_o|\bar{H}|^2 + \frac{1}{4}\epsilon_o\bar{E}^*\cdot\frac{\partial(\omega\bar{\bar{K}})}{\partial\omega}\cdot\bar{E}\right]da} \equiv \frac{\langle P_e\rangle + \langle P_m\rangle}{\langle W\rangle}. \tag{31}$$

Therefore Eq. 31 is applicable even when $\bar{\bar{K}}$ is an operator.

For $a \neq 0$ we may derive the expression for the average power density (which is unique[7]) from Eq. 22. Equation 22 is valid for any $\bar{\bar{K}}$ tensor. When our system is lossless and a conservation principle for the time-averaged power may be derived for it, we have

$$aP_e = -aP_M. \tag{32}$$

By use of Eq. 22, we get

$$P_M = \frac{\omega}{a}\,\mathrm{Im}\,U_{\epsilon a}. \tag{33}$$

Equation 33 is valid for $a \neq 0$. For $a \to 0$ we find

$$\lim_{a\to 0} P_M = -\int \frac{1}{4}\epsilon_o \bar{E}^*\cdot\frac{\partial(\omega\bar{\bar{K}}_h)}{\partial}\cdot\bar{E}\,da,$$

which checks with the well-known result for $a = 0$.[6]

P. E. Serafim, A. Bers

References

1. P. E. Serafim, Interaction between an electron beam and plasma, Quarterly Progress Report No. 64, Research Laboratory of Electronics, M.I.T., January 15, 1962, pp. 95-103.

2. A. Bers, Electromagnetic Waves in Passive and Active Systems, Course 6.637 Lecture, M.I.T., Spring 1962, pp. 38-43.

3. R. J. Briggs and A. Bers, Transverse free waves on electron beams, Quarterly Progress Report No. 67, Research Laboratory of Electronics, M.I.T., October 15, 1962, pp. 35-43.

4. A. A. Th. M. Van Trier, Appl. Sci. Research B3, 305 (1953).

5. W. P. Allis, S. J. Buchsbaum, and A. Bers, Waves in Anisotropic Plasmas (The M.I.T. Press, Cambridge, Mass., 1963), pp. 135-136, give these expressions as upper case letters.

6. W. P. Allis, S. J. Buchsbaum and A. Bers, op. cit.

7. D. L. Bobroff, H. A. Haus, and J. W. Klüver, On the small signal power theorem of electron beams, J. Appl. Phys. 33, 2932-2942 (1962).

D. INTERACTION OF AN ELECTRON BEAM WITH IONS IN A WARM PLASMA OF FINITE TRANSVERSE DIMENSIONS

It has been shown that a one-dimensional model predicts a strong interaction of an electron beam with the ions of a plasma when the plasma electrons are sufficiently warm.[1] The interaction is of the reactive-medium type, and it occurs when the beam space-charge wavelength is less than the plasma Debye wavelength. The present report is concerned with the extension of these results to a beam-plasma system with finite transverse dimensions.

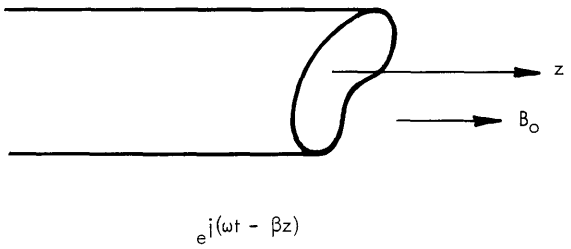

Fig. XII-17. Beam-plasma system.

It is assumed that both the beam and the plasma are homogeneous, and fill a cylindrical waveguide structure (Fig. XII-17). The beam moves with unperturbed velocity, v_o, parallel to a large magnetic field, B_o, which constrains electrons to motion along the field lines. The ions are assumed to be cold; however, transverse motion of the ions is allowed. When the quasi-static assumption is made, it is found that the potential satisfies the two-dimensional Helmholtz equation

$$\nabla_T^2\phi + p^2\phi = 0, \tag{1}$$

where ∇_T^2 is the Laplacian operator in the transverse plane. Also

$$p^2 = -\beta^2\frac{K_{\parallel}}{K_{\perp}}, \tag{2}$$

where

$$K_{\parallel} = 1 - \frac{\omega_{pi}^2}{\omega^2} - \omega_{pe}^2\int\frac{f_o(v_z)\,dv_z}{(\omega-\beta v_z)^2} - \frac{\omega_{pb}^2}{(\omega-\beta v_o)^2} \tag{3}$$

$$K_{\perp} = 1 - \frac{\omega_{pi}^2}{\omega^2 - \omega_{ci}^2} \tag{4}$$

and all symbols have been defined previously.[1]

As in the one-dimensional case, strong interaction with ions is expected only when

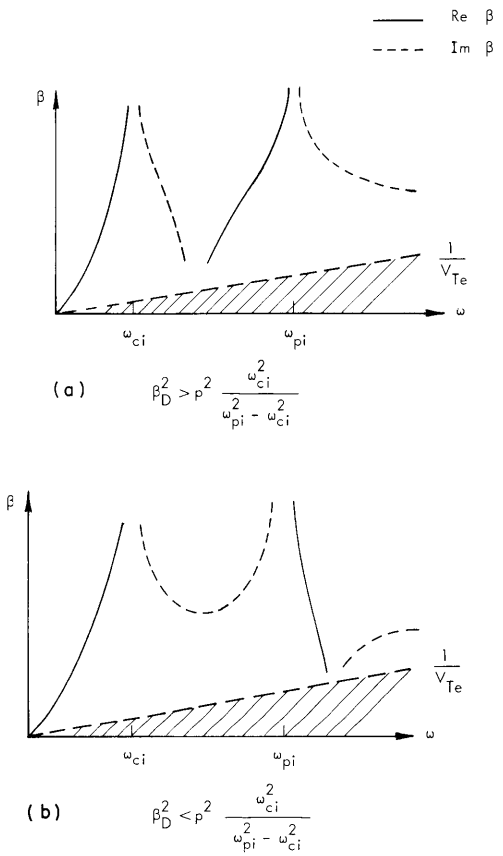

Fig. XII-18. Dispersion in a hot electron plasma.

$v_o \ll V_{Te}$, where V_{Te} is the average thermal velocity of the plasma electrons. Therefore, attention will be restricted to the range in which $\omega \ll \beta V_{Te}$. In this limit,

$$K_{\parallel} \approx 1 - \frac{\omega_{pi}^2}{\omega^2} + \frac{\omega_{pe}^2}{\beta^2 V_{Te}^2} - \frac{\omega_{pb}^2}{(\omega - \beta v_o)^2}. \tag{5}$$

For the plasma in the absence of the beam, the dispersion relation can be written as

$$\beta^2 = -\frac{\beta_D^2 + p^2 K_\perp}{1 - \frac{\omega_{pi}^2}{\omega^2}}, \tag{6}$$

where $\beta_D = \omega_{pe}/V_{Te}$ is the Debye wave number. This dispersion is illustrated in Fig. XII-18 for $\omega_{ci} < \omega_{pi}$. In the limit $V_{Te} \to \infty$, the dispersion becomes identical to that of a cold ion cloud, as would be expected.[2] Normally, however, for reasonable electron temperatures, the resonance at ω_{pi} belongs to a forward wave.

The dispersion equation for the beam-plasma system is a 4th-order equation in β.

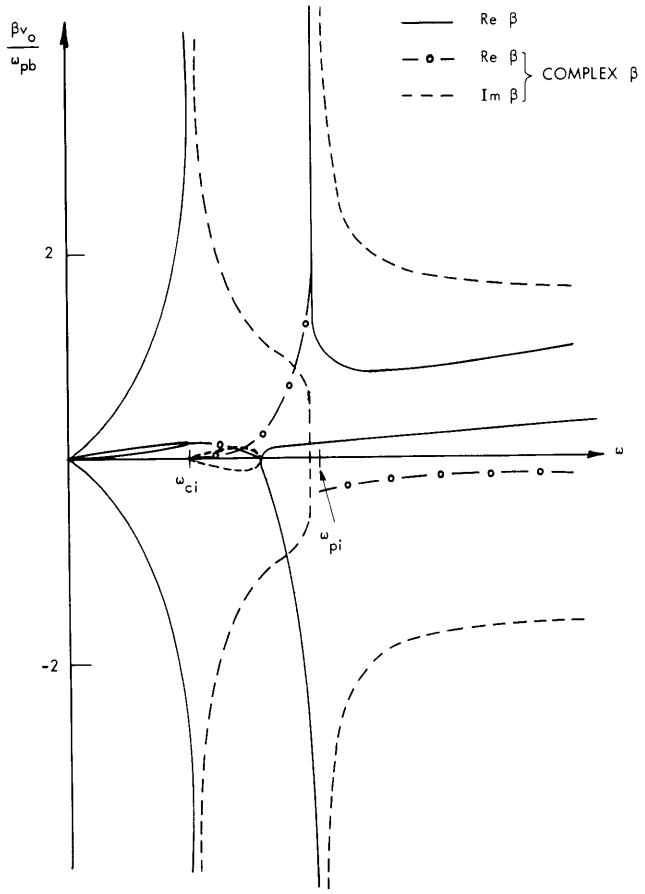

Fig. XII-19. Dispersion for $\frac{n_b}{n_p}\frac{T_e}{2V_o} = 0.5$.

The results of some computations are shown in Figs. XII-19, XII-20, XII-21 for protons with $\beta_{pb}^2 = p^2$, $n_b = 10^{-2}\, n_p$, and $\omega_{pi} = 2\omega_{ci}$, and for values of the "temperature"

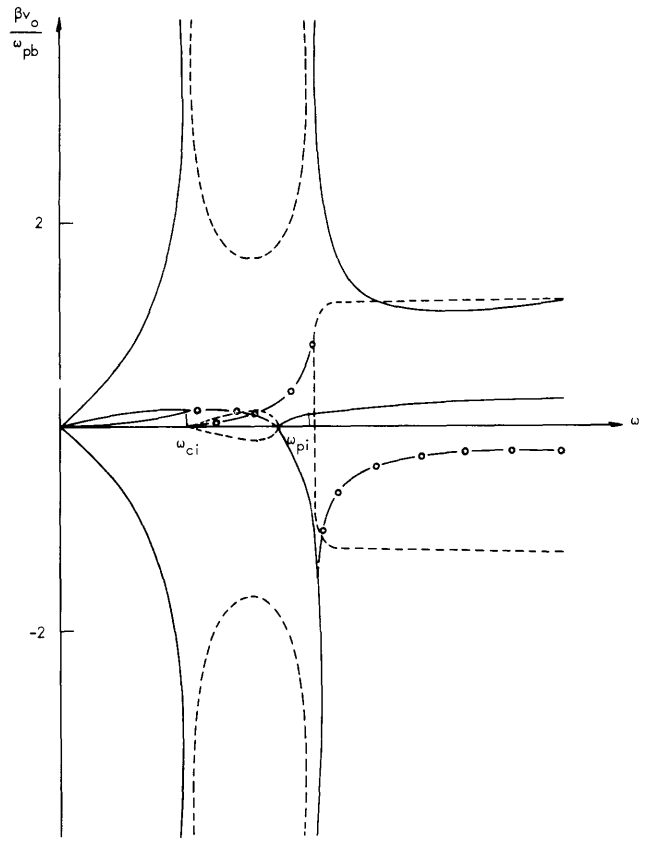

Figure XII-20.
Dispersion for $\frac{n_b}{n_p}\frac{T_e}{2V_o} = 1$.

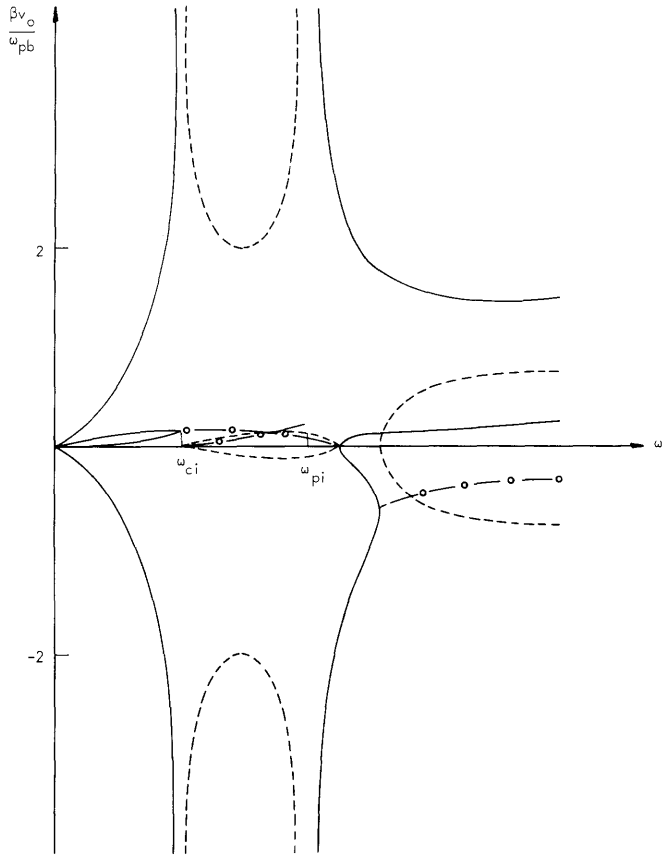

Figure XII-21.
Dispersion for $T_e = \infty$.

parameter $\frac{n_b}{np}\frac{T_e}{2V_o} = \frac{\lambda_D^2}{\lambda_{pb}^2}$ equal to 0.5, 1, and ∞. The condition for obtaining real β for $\omega > \omega_{pi}$ now is

$$\beta_{pb}^2 + p^2 \frac{\omega_{ci}^2}{\omega_{pi}^2 - \omega_{ci}^2} > \beta_D^2, \tag{7}$$

in agreement with the numerical computations.

The interpretation of these plots by means of the amplifying criterion that was recently derived by the authors is being investigated. It is interesting to note that the complex root of β with Im $\beta \to \infty$ at $\omega = \omega_{pi}$ carries negative kinetic power if the Debye wave number in the range

$$\beta_{pb}^2 + p^2 \frac{\omega_{ci}^2}{\omega_{pi}^2 - \omega_{ci}^2} > \beta_D^2 > p^2 \frac{\omega_{ci}^2}{\omega_{pi}^2 - \omega_{ci}^2} . \tag{8}$$

This raises a strong suspicion that this wave is an amplifying wave with a spatial growth rate tending to infinity, under the condition of Eq. 8.

R. J. Briggs, A. Bers

References

1. R. J. Briggs and A. Bers, Electron-beam interactions with ions in a warm plasma, Quarterly Progress Report No. 69, Research Laboratory of Electronics, M.I.T., April 15, 1963, pp. 65-73.

2. L. D. Smullin and P. Chorney, Proc. International Symposium on Electronic Waveguides (Polytechnic Institute of Brooklyn, New York, 1958), pp. 229-247.

E. TEST AND MODIFICATION OF LARGE SUPERCONDUCTING SOLENOID

The large superconducting solenoid described at length in previous reports[1-4] has been completed and temperature-cycled twice. The coils could not be cooled below the superconducting transition temperature; the system has a repairable thermal short.

To give an idea of what happened, we summarize the pertinent assembly details. Figure XII-22 shows a cross section of one end of the magnet. The view is not drawn to scale so that the critical small dimensions will be visible. Unlabeled dimensions have no relevance to the present discussion. Some vacuum flanges and other detail in irrelevant places are not shown. All radiation shields are held off surfaces by nylon studs; bolt and screw locations are shown by simple lines, as pins.

The 0.25-in. span between magnet coils and shield H was originally intended to be larger ($\geq$0.5 in.), but the individual magnet coils (24 of them) spread axially when wound, and thus reduced the clearance and created part of our problem.

As the coils cool, the supporting column shrinks almost 0.25 in.; the spacings shown are for the system "cold." The system was aligned before evacuation and cooling. During cooling, however, the supporting columns shrank unevenly, moving the nitrogen shield to the left, and the magnet coils to the right. Thus the magnet coil structure touched the shield H; also, the coils swung (out of the paper in the sketch) and a metallic connection was made between the coils and the side of the nitrogen shield F. Total motion was approximately 0.25 in. The coils cooled to approximately 15°K (estimated) through circulation of helium through the pipes, K, attached to the coil. By forcing excess helium through the system, the thermal switches at point J could be made superconducting

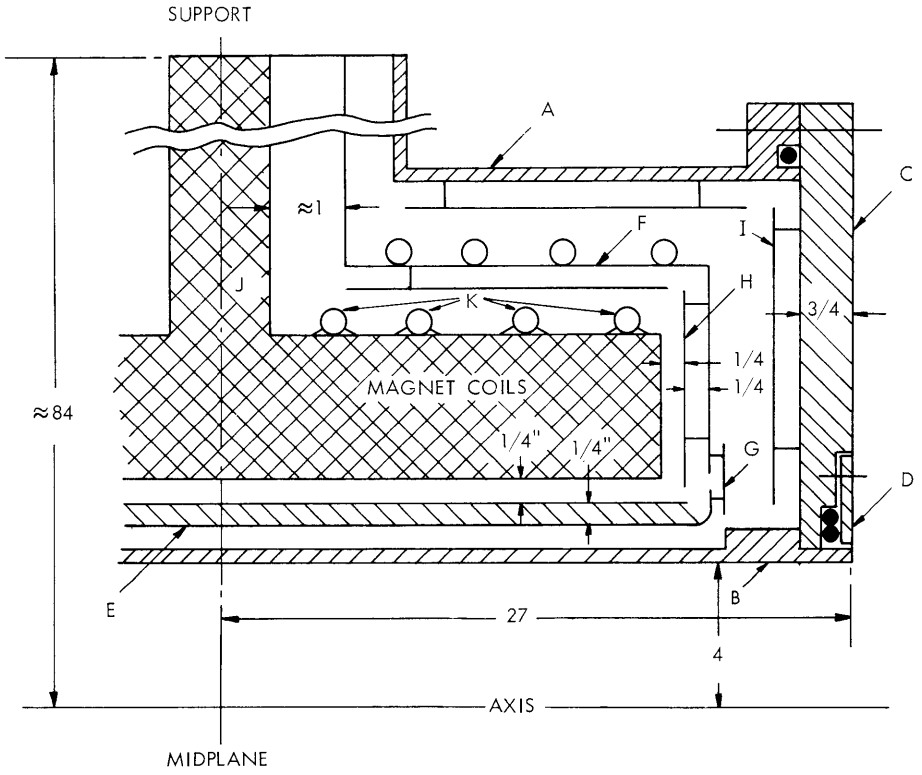

Fig. XII-22. Sketch (not to scale) of cross section of magnet, upper right quadrant, showing critical dimensions, in inches.
A. Cylindrical vacuum wall, O.D.
B. Cylindrical vacuum wall, I.D.
C. End flange
D. Sealing ring and O-rings, I.D.
E. Nitrogen shield, including cooling pipes and radiation shield, I.D.
F. Nitrogen shield, O.D. and end flanges
G. Annular joining ring, nitrogen shield
H. Radiation shield, supported off end of nitrogen shield
I. Radiation shield, supported off end of vacuum wall
J. Position of thermal switches
K. Helium precooling line

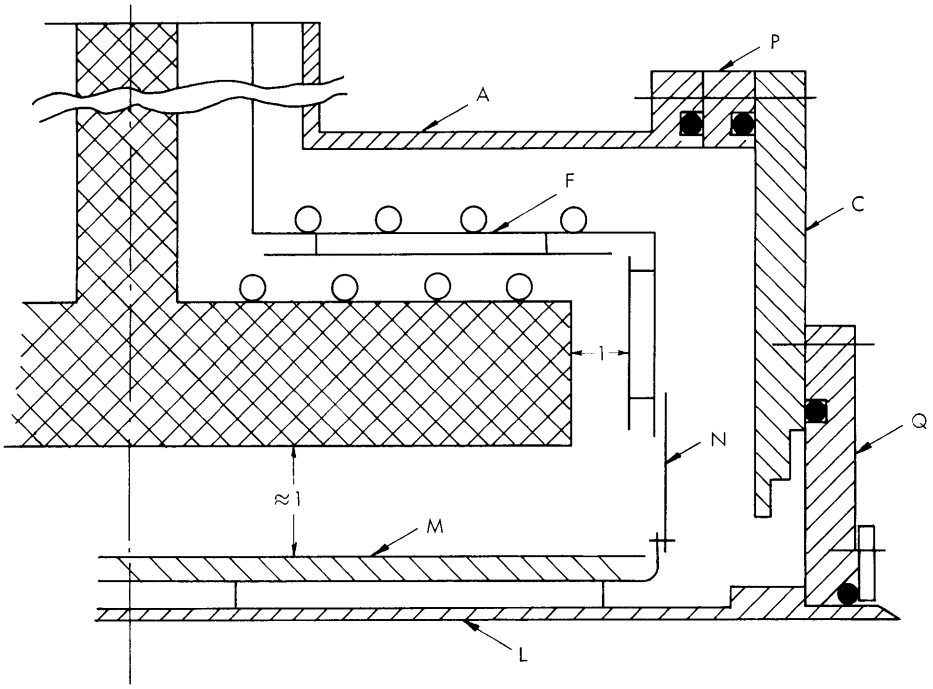

Fig. XII-23. Modification to magnet.
L. New vacuum wall, I. D.
M. New nitrogen shield, I. D.
N. Thermal sealing ring
P. Axial spacer
Q. End flange adaptor

because the helium line ends at a reservoir there.

No contact between the nitrogen shield and the outer wall took place. For the coils and nitrogen shield together, the thermal isolation is good, even at a pressure of 2×10^{-5} mm Hg. Temperature rise was 10-15°K/day at 77°K.

Heat transfer from the cooling pipes K to the magnet coils has been recalculated and found more than adequate for initial solenoid tests. The largest thermal impedance lies in the coils themselves, where the wire is insulated by 0.001-in. nylon and 0.010-in. mylar between wire layers. The cooling time constant is ~100 sec at 20°K, and will be higher near 4°K. Times of 100-1000 sec are acceptable. It is calculated that the thermal contacts that had been found could reasonably account for the 25-watt heat input to the magnet coil (as determined by helium enthalpy rate into and out of the magnet coil structure).

A relatively simple modification is planned to correct the difficulty at the cost of 1 inch in working radius. The modification is sketched in Fig. XII-23 (not drawn to scale). The vacuum cylinder A, the end plate C, and the nitrogen shield F are retained. These are the most expensive items. A new I.D. vacuum wall L, of 3-in. radius, has been made, and a new inner nitrogen shield M is attached to it with nylon studs. Cooling is brought to it by a pipe and bellows from shield component F. Radial clearance to the

magnet coil I. D. is now almost 1 inch. Also, the end of shield F is cut off, and a cylindrical strip is inserted to extend F axially 0.75 inch. The nitrogen shielding is completed by a new annular copper ring N, bolted to M, and loosely pinned to the end wall F.

The axial modification requires a ring spacer P on the outside diameter, and the radial modification requires plate Q, which clamps to C with an O-ring and holds the I. D. wall L. These modifications have been made at both ends of the magnet.

Dimensions at the outer diameters (magnet coils radially to F, for example) are large and require no modification.

D. J. Rose, L. M. Lidsky, E. Thompson, J. Woo

References

1. D. J. Rose and L. J. Donadieu, Quarterly Progress Report No. 62, Research Laboratory of Electronics, M. I. T., July 15, 1961, p. 68.

2. L. J. Donadieu and D. J. Rose in Proc. International Conference on High Magnetic Fields, edited by H. Kolm (The M. I. T. Press, Cambridge, Mass., 1961), pp. 358-369.

3. L. J. Donadieu, Large-volume superconducting solenoid, Quarterly Progress Report No. 66, Research Laboratory of Electronics, M. I. T., July 15, 1962, p. 139.

4. L. J. Donadieu, Superconducting solenoid, Quarterly Progress Report No. 68, Research Laboratory of Electronics, M. I. T., January 15, 1963, p. 86.

F. ORBIT STABILITY IN THE CORKSCREW

1. Introduction

The transfer of longitudinal to transverse kinetic energy in a helically perturbed magnetic field has been demonstrated experimentally by Wingerson,[1] Dreicer et al.,[2] and discussed in detail by Wingerson, Dupree, and Rose.[3] The energy transfer depends on a resonance of the position and velocity of the particle with the orientation and magnitude of the perturbing magnetic field. It has been shown,[3] and is now shown in greater detail in this report, that this resonance is stable to first order, that is, a particle displaced from the stable orbit will oscillate about the position of stability. We address ourselves here to the question of second-order stability – do the oscillations about the stable orbit grow or decay?

It will be shown in this report that the linearized equations of motion predict growth of the oscillations in an axially decelerating corkscrew and decay of the oscillations in an axially accelerating corkscrew. The equations of motion for perturbations about the stable orbit in an optimized (in the sense explained elsewhere[3]) corkscrew are displayed. Numerical solutions of these equations are presented, and the results discussed.

2. Linearized Equations of Motion

For the coordinate system of Fig. XII-24, the orbital equations for v, the azimuthal velocity, and χ, the relative azimuthal angle, for total energy E_o, are

$$\frac{dv}{dz} = \omega_r(r, z) \cos \chi \tag{1}$$

$$\frac{d\chi}{dz} = -\frac{2\pi}{P(z)} + \frac{\omega_z}{[U-v^2]^{1/2}}, \tag{2}$$

where $\omega_r = qB_r/m$, $\omega_z = qB_z/m$, $U = 2E_o/m$, and $P(z)$ is the local pitch length. The assumption is made that the radial velocity, but not the radial position, can be ignored.

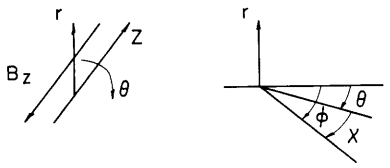

θ = ANGULAR POSITION OF FIELD MAXIMUM

φ = ANGULAR POSITION OF PARTICLE

Fig. XII-24. Coordinate system for derivation of the orbital equations.

If $v = v_o + v_1$ and $\chi = \chi_o + \chi_1$, where $v_o(z)$ and $\chi_o(z)$ refer to the unperturbed orbit of the particle, then to first order in the perturbation variables

$$\frac{dv_1}{dz} = -\omega_r(r, z) \sin \chi_o \chi_1 \tag{3}$$

$$\frac{d\chi_1}{dz} = -\frac{2\pi}{P(z)} + \frac{\omega_z v_o v_1}{\left[U-v_o^2\right]^{3/2}}. \tag{4}$$

Equations 3 and 4 yield a second-order differential equation for χ,

$$\frac{d^2\chi_1}{dz^2} + g(z)\frac{d\chi_1}{dz} + h(z)\chi_1 = 0, \tag{5}$$

where

$$g(z) = \frac{3}{P}\frac{dP}{dz} - \frac{1}{v_o}\frac{dv_o}{dz} \tag{6}$$

and

$$h(z) = \frac{(2\pi)^3 v_o(z) \omega_r(r, z) \sin \chi_o}{\omega_z^2 P^3(z)}. \tag{7}$$

The coefficient of χ_1 is positive for both accelerating and decelerating corkscrews. For deceleration with $\omega_r > 0$, Eq. 1 limits the particle position to the first or fourth quadrant (that is, the azimuthal velocity must increase with z). A particle in the first quadrant displaced forward in χ will be decelerated less strongly, move with too high z velocity relative to the local pitch and so move back toward the original position. Similarly, a particle displaced backward in χ will suffer stronger deceleration and move toward the original position. On the other hand, a particle in the fourth quadrant will move in the direction of the displacement, and rapidly fall out of synchronism. An accelerating corkscrew, with χ_o necessarily in either the second or third quadrant, is stable (in the sense that small displacements lead to oscillatory motion about the origin of the displacement) only in the second quadrant. By the same arguments, if the direction of the perturbing field is reversed, then χ_o must be in the third or fourth quadrant for oscillatory stability. In any of these cases, h(z) is positive.

Because h(z) is a monotonically varying, always positive function of z, the stability of the oscillations depends only on the sign of g(z). Equation 6 shows g(z) to be negative (growing oscillations) for decelerating corkscrews, and to be positive (decaying oscillations) for accelerating corkscrews.

3. Optimum Corkscrew

Wingerson, Dupree, and Rose demonstrate that the scattering losses for trapped particles are reduced for a corkscrew in which $dv_\perp/dz \to 0$ at both ends. We shall consider first-pass particle motions in such a system. Particularly, we demand that the perpendicular velocity in the unperturbed orbit, $v_{\perp o}$, be given by

$$v_{\perp o} = a v_o \sin^2\left(\frac{\pi z}{2L}\right), \tag{8}$$

where a is a parameter describing the total change in perpendicular velocity, v_o is the TOTAL (vector) velocity of the particle, and the corkscrew is assumed to be of length L. The resonance condition gives

$$P(z) = \frac{2\pi v_o}{\omega_z}\left[1 - a^2 \sin^4\left(\frac{\pi z}{2L}\right)\right]^{1/2} \tag{9a}$$

$$= P_o\left[1 - a^2 \sin^4\left(\frac{\pi z}{2L}\right)\right]^{1/2}. \tag{9b}$$

Equations 1, 8, and 9b combine to fix the necessary variation of $\omega_r(r, t)$:

$$\omega_r(r, z) = \frac{\left(\frac{\pi a}{2L}\right) \sin\left(\frac{\pi z}{L}\right)}{G(\chi_o, z) \cos \chi_o}\left\{I_o\left[\frac{2\pi r}{P(x)}\right] + I_2\left[\frac{2\pi r}{P(z)}\right]\right\}, \tag{10}$$

where

$$G(r_o, z) = G\left(\frac{v_{\perp o}}{\omega_z}, z\right) = I_o\left[\frac{2\pi v_{\perp o}(z)}{\omega_z P(z)}\right] + I_2\left[\frac{2\pi v_{\perp o}(z)}{\omega_z P(z)}\right]. \tag{11}$$

The algebra is simplified by introducing the new variables $x = \pi z/2L$, $v = v_\perp/v_o$, and $p(x) = P(x) = P_o$. In this notation,

$$\frac{dv}{dx} = \frac{a \sin 2x}{G(v_{\perp o}, x) \cos \chi_o} \cdot G(v, x) \cos \chi \tag{12}$$

and

$$\frac{d\chi}{dx} = \frac{4L}{P_o}\left[\frac{1}{(1-v^2)^{1/2}} - \frac{1}{p(x)}\right]. \tag{13}$$

We take advantage of the fact that the unperturbed orbit is known and rewrite the equations in terms of deviations from this orbit; that is, for $\chi_1(x) = \chi(z) - \chi_o$ and $v_1(z) = v(z) - v_o(z)$.

$$\frac{dv_1}{dx} = a \sin 2x\left\{\frac{G(v_o+v_1, x)}{G(v_o, x)}(\cos \chi_1 - \tan \chi_o \sin \chi_1) - 1\right\} \tag{14}$$

$$\frac{d\chi_1}{dx} = \frac{\gamma}{p(x)}\left\{\frac{1}{1 - \left[\frac{2a \sin^2 xv_1 + v_1^2}{p^2(x)}\right]^{1/2}} - 1\right\}. \tag{15}$$

where

$$p(x) = [1 - a_2 \sin^4(x)] \tag{16}$$

$$G(v_o+v_1, x) = I_o\left[\frac{a \sin^2(x) + v_1}{p(x)}\right] + I_2\left[\frac{a \sin^2(x) + v_1}{p(x)}\right] \tag{17}$$

$$\gamma = 4L/P_o. \tag{18}$$

Except for the slowly varying ratio of the G's, Eqs. 14 and 15 are first order in deviations from equilibrium. The oscillations about the unperturbed orbit are thus separated from the equations of the orbit itself, and can be studied with far greater accuracy. Notice also that no additional approximations have been made (that is, these equations are not linearized).

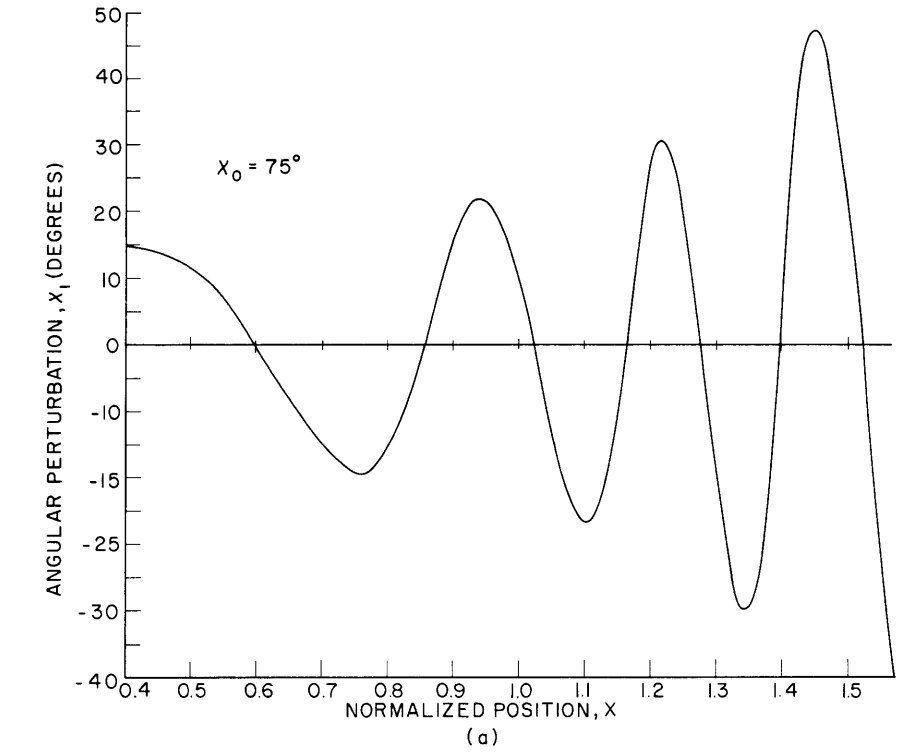

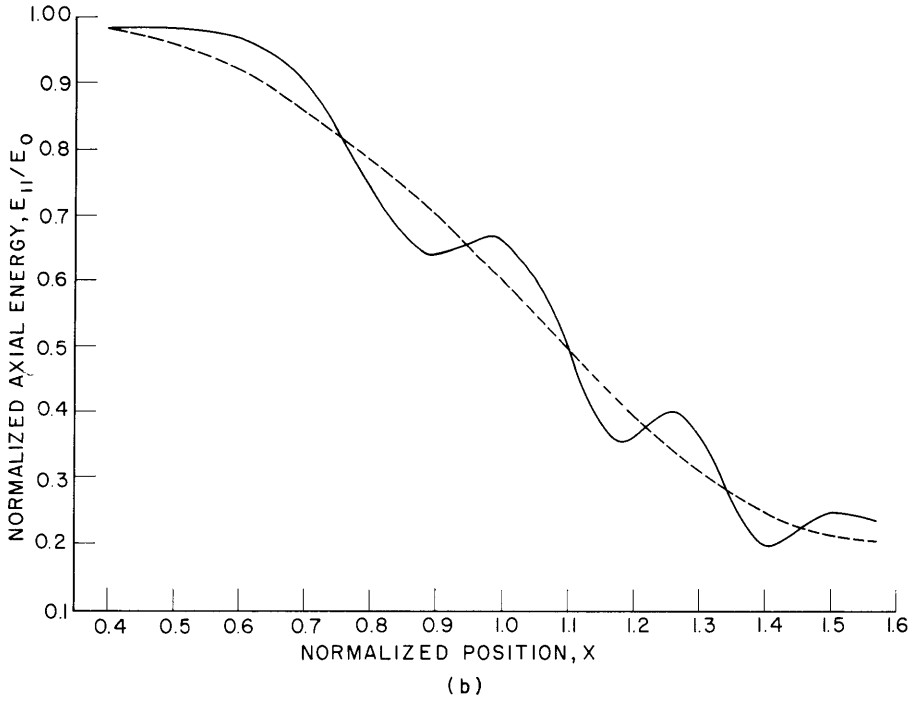

Fig. XII-25. (a) Angular deviation of particle position from the equilibrium orbit as a function of the normalized distance, x. $x = \pi z/2L$, where z is the position of the particle, and L is the length of the helical field.
(b) Normalized z-directed energy of the particle as a function of x. The dashed line illustrates the behavior of an unperturbed particle.

Equations 14 and 15 were solved numerically by four-step Runge-Kutta integration. The results presented below were all computed by using a normalized distance increment of 10^{-3} (1570 steps for a single traverse). The results at the end of a complete pass were changed at most by 2 parts in the fifth significant figure for distance increments of 10^{-2} and 10^{-4}. A complete traverse, including computation and print-out of position, velocity, and energy at 157 points, requires approximately 21 seconds of IBM 7090 computer time.

4. Numerical Results

The equations of the system are characterized by three parameters:

α the ratio of exit azimuthal velocity to the total velocity of the particle;

γ a number proportional to the number or "corkscrew turns" in the system ($\gamma = 4L/P_o$); and

χ_o the particle phase for which the corkscrew was designed.

Numerical computations were carried out for systems comparable to the electron corkscrew experiments of Wingerson and Dreicer ($\gamma = 20$), and for the more finely tuned systems of ultimate interest. We considered alpha values of 0.500 and 0.894 (25 per cent and 80 per cent of the energy in transverse motion at the exit), gamma values of 50 and 100, and design angles of 30°, 45°, 75°, and ±135°. The last two values are for the stable and unstable quadrants for an accelerating corkscrew ($\pi/2 \leq x \leq \pi$). The gamma values are those of an electron corkscrew with, for example, 200-gauss main axial field, 1600-volts injection energy, and 53-cm or 106-cm length. The number of turns depends on the value of α. For $\alpha = 0.894$ and $\gamma = 100$, this number is approximately 52. Some typical results are discussed below for this last case.

(a) Decelerating Corkscrews

A corkscrew as defined by Eq. 9 is decelerating for $0 \leq x \leq \pi/2$, and is phase stable for χ_o in the first quadrant. Figure XII-25a shows the effect of a 15° perturbation in the angular position at $x = 0.4$. As expected, the oscillations grow in magnitude and frequency along the corkscrew. Figure XII-25b is a plot of axial energy during these oscillations compared with the smooth deceleration of an unperturbed particle. The angular-position perturbation leads to an energy perturbation because a particle in the first quadrant displaced forward in χ is subject to a smaller radial field, and is decelerated less strongly than an unperturbed particle.

Figure XII-26 illustrates the effect of an energy perturbation ($\Delta E = -0.06$) at the same position. The phase angle χ at various axial positions is marked off along the curve. The particle was lost when χ became more negative then -45° at a time when

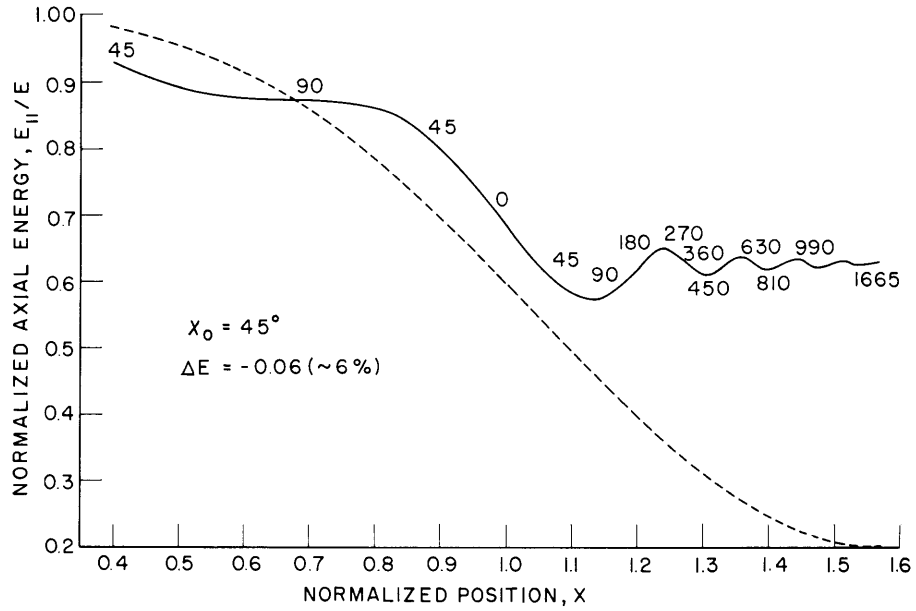

Fig. XII-26. Normalized z-directed energy versus x. The particle phase, χ, is plotted as a running parameter.

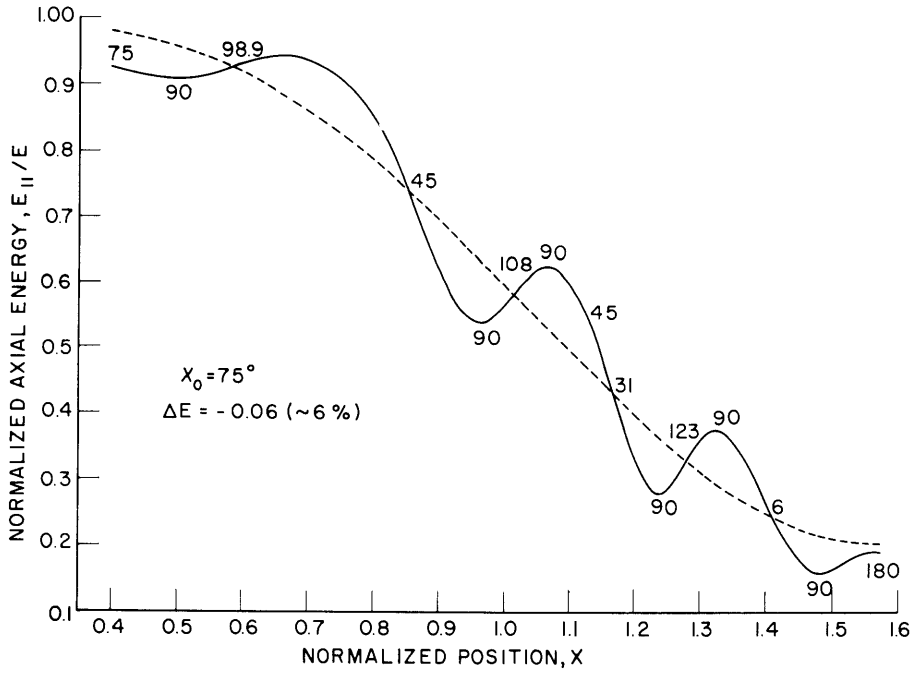

Fig. XII-27. Normalized z-directed energy versus x. The conditions for this case differ from those of Fig. XII-26 only in the value of χ_0. χ is the running parameter.

the axial velocity was higher than the axial velocity for an unperturbed particle. The radial field for $\chi < -45°$ is smaller than the design field, and the particle slipped even farther behind in phase. The radial field is negative for $-3\pi/2 \leq \chi \leq \pi/2$, and the particle was accelerated. It continued to slip behind in phase because $\frac{d\phi}{dz} = \frac{1}{v_z}\frac{d\phi}{dt}$ was everywhere smaller than $d\theta/dz$ as defined by the corkscrew windings. Successive cycles of acceleration ($-3\pi/2 + n\pi \leq \chi \leq \pi/2 + n\pi$) and deceleration ($-\pi/2 \pm n\pi = \chi = \pi/2 \pm n\pi$) followed, but the effect of each became smaller because the particle spent less time in the successively shorter sections.

Figure XII-27 is a plot of the same case for an initial design phase, χ_o, of 75°. Two factors cause this situation to be more stable than that in Fig. XII-26. First, the particle must slip farther back in phase to see a radial field weaker than the design field. Second, and more important, the ratio of maximum radial field to design field is larger for $\chi_o = 75°$ than it is for $\chi_o = 45°$. $[\omega_r(\chi=0) = 1.4\,\omega_r(45°) = 3.9\,\omega_r(75°)]$. The improved stability is, of course, accompanied by increased perturbation of previously trapped particles.

(b) Accelerating Corkscrews

The pitch equation (9) describes an accelerating corkscrew for $\pi/2 \leq x \leq \pi$. A system with parameters identical to the decelerating corkscrew discussed above ($a = 0.894$, $\gamma = 100$) was investigated for the case $\chi_o = 135°$ and $x > \pi/2$. The effect of an angular perturbation at the entrance is depicted in Fig. XII-28. The result of an identical

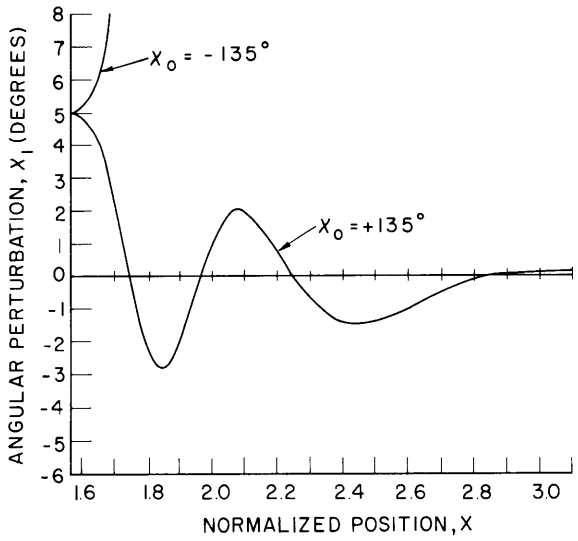

Fig. XII-28. Angular deviation versus x for an accelerating corkscrew. Note that $\pi/2 \leq x \leq \pi$ for this case.

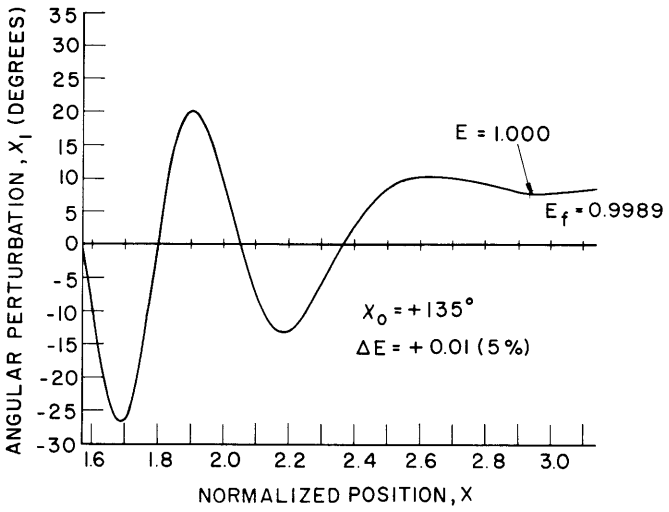

Fig. XII-29. Angular deviation versus x for the corkscrew of Fig. XII-28. In this case, the initial perturbation was in energy.

perturbation for a particle in the unstable accelerating quadrant ($\chi_0 = -135°$) is shown. As predicted, the oscillations of the particle in the proper quadrant are rapidly damped. The angular oscillations resulting from a 5 per cent energy perturbation at the entrance are shown in Fig. XII-29. The particle was completely unwound at the local minimum at x = 2.95. The longitudinal energy at the exit was 0.9989 of the total energy.

5. Conclusions

The numerical results presented for the decelerating corkscrew thread the passage between the rock of experiment — the corkscrew decelerates particles — and the whirlpools of intuition and linearized theory — the decelerating corkscrew is unstable to growing oscillations. The corkscrew is indeed unstable, but not too unstable. The numerical results agree nicely with the experimental work of Dreicer and his co-workers[2] in showing that a small energy spread at the exit is accompanied by a large spread in exit phase. The size of the "acceptance hole" at the corkscrew entrance is also in agreement with experiment (± ~10 per cent in energy, ± ~30° in phase).

Cases similar to that shown in Fig. XII-26, which indicates that particles can be partially wound up to an extent determined by their initial deviation from the stable orbit, call into question an earlier conclusion that the optimum system would consist of a finely tuned corkscrew with a very carefully matched injection system. It is likely that an injection system with a moderate spread in particle velocity (resulting in a wide spread in energy and phase at the corkscrew exit) would circumvent many of the difficulties that plague devices with highly ordered particle motions.

The accelerating corkscrew presents intriguing possibilites for injection into

"closed" toroidal systems. In the simple form discussed in this report it is capable of placing particles on the axis of a toroidal system whose minor radius is equal to the cyclotron radius of a particle with total velocity in the transverse direction. Injection into a field extending over several cyclotron radii is more desirable. Modifications of the accelerating corkscrew to accomplish this end are under study.

L. M. Lidsky

References

1. R. C. Wingerson, Phys. Rev. Letters 6, 446 (1961); R. C. Wingerson, Quarterly Progress Report No. 60, Research Laboratory of Electronics, M. I. T., January 15, 1961, pp. 59-65.

2. H. Dreicer et al., Nuc. Fus. 1962 Supplement I, p. 299, 1962.

3. R. C. Wingerson, T. H. Dupree, and D. J. Rose (unpublished material).

G. FUSION REACTION BLANKET EXPERIMENT: ANALYSIS OF THRESHOLD-DETECTOR DATA

The neutron-energy spectra in mock-ups of a tritium regenerating blanket to surround a power-producing deuterium-tritium-cycle thermonuclear reactor will be measured by means of the following threshold reactions: $U^{238}(n, f)$, $P^{31}(n, p)Si^{31}$, $Fe^{56}(n, p)Mn^{56}$, $I^{127}(n, 2n)I^{126}$, and $F^{19}(n, 2n)F^{18}$. A description of the experimental arrangement and of the physical properties of the threshold-detector foils has been given previously.[1] The method of analysis of the activities from these reactions for the purpose of determining the neutron spectrum, generalized to the case of N different threshold reactions, is given in this report.

The problem is the solution of N simultaneous integral equations for the neutron spectrum $\phi(E)$:

$$T_j = \int \phi(E)\sigma_j(E)\, dE, \qquad (j=1, 2, \ldots, N). \tag{1}$$

Here, the T_j is the activation rate per atom of the j^{th} threshold detector corrected for decay, and $\sigma_j(E)$ is the activation cross section. The range of all integrals in this discussion is from the lowest threshold energy to the maximum energy to be expected in the experiment. Since the general solution of Eq. 1 is intractable, some assumptions about the $\sigma_j(E)$ and the neutron-energy spectrum $\phi(E)$ must be made. The method of Lanning and Brown[2] has been chosen for two reasons: it is relatively simple, and it allows additional knowledge of the spectrum – in this case, from calculations made with machine codes developed by Impink[3] – to be taken into account by means of a weight function w(E).

In this method $\phi(E)$ is expanded as a product of $w(E)$ times a weighted sum of polynomials $p_i(E)$:

$$\phi(E) \sim w(E) \sum_{i=1}^{N} a_i p_i(E). \tag{2}$$

The polynomials $p_i(E)$ (of degree i-1) are chosen so that

$$\int p_i(E) p_k(E) w(E)\, dE = \delta_{ik}. \tag{3}$$

The $\sigma_j(E)$ are approximated as a Fourier expansion of the $p_i(E)$:

$$\sigma_j(E) \sim \bar{\sigma}_j(E) = \sum_{i=1}^{N} \tau_{ji} p_i(E), \tag{4}$$

where

$$\tau_{ji} = \int p_i(E) \sigma_j(E) w(E)\, dE. \tag{5}$$

The method gives a least-squares fit to the cross-section data:

$$\int w(E) \left[\sigma_j(E) - \bar{\sigma}_j(E) \right]^2 dE = \text{minimum}. \tag{6}$$

If we use these equations, the activation of the j^{th} foil is given by

$$T_j = \sum_{j=1}^{N} \tau_{ji} a_i, \qquad (j=1, \ldots, N). \tag{7}$$

The N equations (7) are solved for the a_i; this operation completes the calculation of all of the parameters that are necessary to determine $\phi(E)$ by Eq. 2.

A Fortran-II program has been written to perform the calculations, and has been tested by using activities computed from spectra calculated by Impink. Two examples are shown in Fig. XII-30 in which the input spectrum is shown with two spectra calculated from Eq. 2 by using two different $w(E)$ for two sets of data. Since only 5 foils are used, the calculated spectrum is dependent on the function chosen for $w(E)$. If the weight function $w(E)$ is chosen to be the input spectrum, of course, the agreement is excellent. As an example of a weight function that has the general shape of the input spectrum, but does not depend directly on the spectrum, a weight function of the form

$$w(E) = (A + BE^J)^{-1} + C \exp(-(E-F)^2/G^2) \tag{8}$$

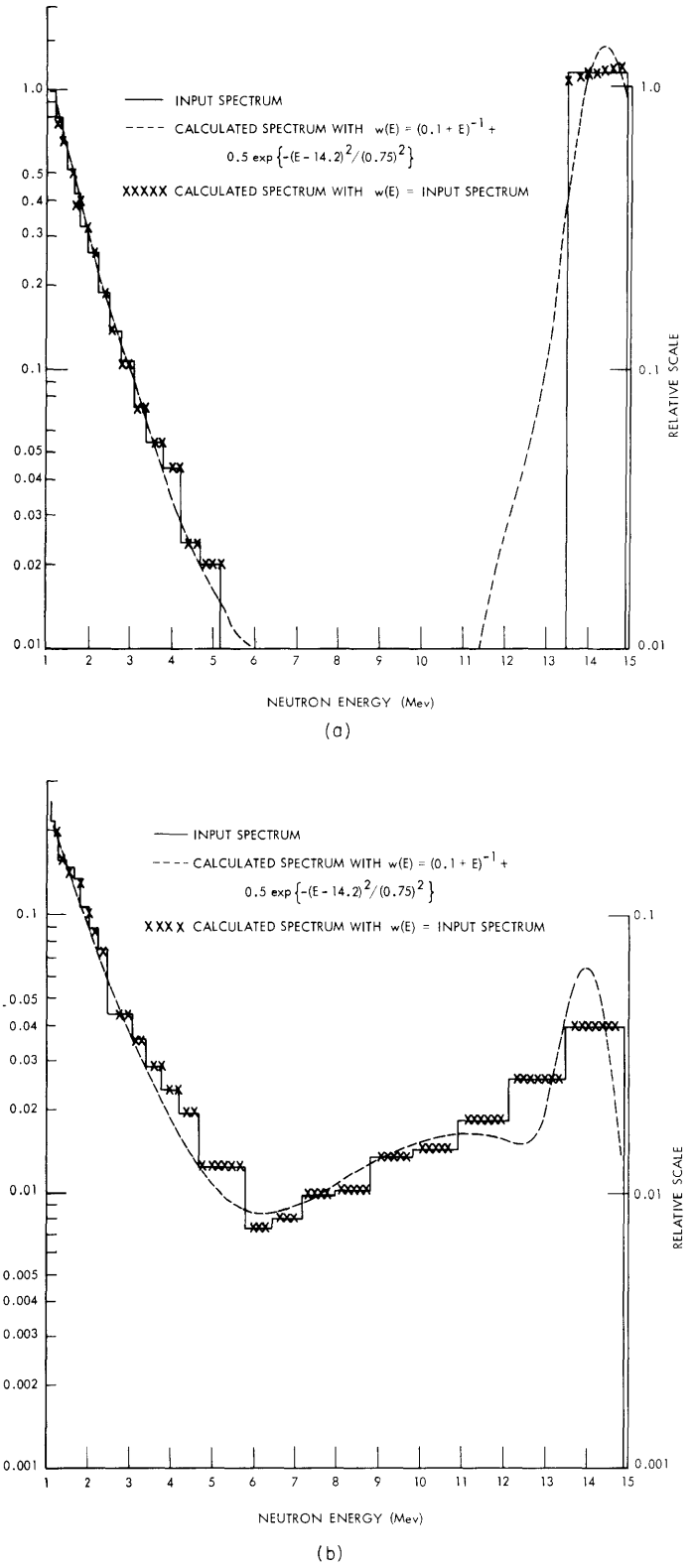

Fig. XII-30. Comparison of spectrum calculated from Eq. 2 with input spectrum calculated from Impink's codes. Data in (a) are from the first wall of the blanket; data in (b) are from a point approximately 20 cm from the first wall.

Table XII-1. Comparison of threshold activities.

Reaction	Threshold energy (Mev)	Used to determine a_i in Eq. 2	Calculated activity[a]	
			From input spectrum	From $\phi(E)$ according to Eq. 2
$U^{238}(n, f)$	1.1	yes	2264.1	2264.1
$P^{31}(n, p)Si^{31}$	1.6	yes	163.65	163.74
$Fe^{56}(n, p)Mn^{56}$	4.5	yes	226.95	226.95
$I^{127}(n, 2n)I^{126}$	9.5	yes	2103.0	2103.0
$F^{19}(n, 2n)F^{18}$	11.1	yes	87.808	87.808
$Al^{27}(n, \alpha)Na^{24}$	6.1	no	208.00	208.75
$Zn^{64}(n, p)Cu^{64}$	1.9	no	421.75	425.69
$Ni^{58}(n, 2n)Ni^{57}$	12.3	no	43.139	42.609

[a]Activity calculated by $T_i = \int \phi(E)\sigma_i(E)\, dE$, where $\sigma_i(E)$ is the cross section, and $\phi(E)$ is the input spectrum, or the spectrum calculated with w(E) from Eq. 8, by using data from Fig. XII-30a.

was chosen. The values of the constants A, B, C, F, and G were chosen somewhat arbitrarily; the fit of the calculated spectrum to the input spectrum is not too dependent upon the choice. Furthermore, the same w(E) gives a good fit to the data at the first wall (Fig. XII-30a), where the peak centered about 14.2 Mev predominates, as well as farther in the blanket (Fig. XII-30b), where this peak has been attenuated, and the intervening energy regions have been filled in by the moderated neutrons.

Tests were also made with w(E) = 1.0. The results showed that the input spectrum is too complicated to be fitted by a fourth-order polynomial: The calculated spectrum, while it did show the trends at the lower and upper regions of the spectrum, oscillated about the origin in the region 6-12 Mev.

In these calculations the assumption was made that the T_j are known exactly, which is not actually true. In a series of test runs, the T_j calculated from the input spectra were varied by fixed amounts. The results showed that the shape of the spectrum calculated from Eq. 2 is most sensitive to the activities of the reactions with intermediate threshold energies: $P^{31}(n, p)$, $Fe^{56}(n, p)$, and especially $I^{127}(n, 2n)$. Increasing or decreasing the activities of the foils with the highest and lowest threshold energies merely increases or decreases the value of the calculated spectrum in the corresponding energy range.

Since these calculations are based on an integral method, information about $\phi(E)$ in regions where it is small (say <0.01 of its maximum value) can be lost in the uncertainties in the method; likewise for $\sigma_i(E)$ in regions where $\phi(E)$ is large. Thus a fairer test of the method is its ability to reproduce activation rates of reactions which were not used in determining the calculated spectrum because in performing the integral $\int \phi(E)\sigma(E)\, dE$ to determine these activities, errors in regions where $\phi(E)$ is small are of less importance. The activities of three such reactions, obtained by integrating the cross section for the reaction with the input and calculated spectra are shown in Table XII-1. The maximum deviation between the activities obtained from the input spectrum, and those obtained from the spectrum calculated with the Gaussian weight function, is approximately 1 per cent.

P. S. Spangler

References

1. P. S. Spangler, Fusion reactor blanket experiment, Quarterly Progress Report No. 69, Research Laboratory of Electronics, M.I.T., April 15, 1963, pp. 81-88.

2. W. D. Lanning and K. W. Brown, Report WAPD-T-138, Bettis Atomic Power Laboratory, Pittsburgh, Pennsylvania, 1961; see also Trans. Am. Nuclear Soc. 4, 267 (1961).

3. A. J. Impink, Neutron Economy in Fusion Reactor Blanket Assemblies, Sc.D. Thesis, Department of Nuclear Engineering, M. I. T., January 1963.

H. EMISSION OF CYCLOTRON HARMONICS FROM PLASMAS

Considerable interest has been stimulated recently by the observation of maxima in the emission and absorption spectrum of plasma at harmonics of the cyclotron frequency.[1] Since the electron energies in the plasmas were nonrelativistic, some mechanism other than pure single-particle cyclotron radiation must be responsible for the observed spectrum. Simon and Rosenbluth[2] have suggested that the radiation is due to electrons whose trajectories pass through sheaths. The electric fields in the sheaths distort the circular Larmor orbits, and the result is the emission of radiation at the cyclotron harmonics.

The qualitative aspects of the observed spectrum can also be produced by another mechanism: the scattering of longitudinal electron waves by the ions. At equilibrium, such scattering produces a relatively smooth bremsstrahlung spectrum, but for a non-equilibrium plasma, the spectrum can be quite different. In particular, for a plasma in a magnetic field, a longitudinal wave traveling perpendicular to the magnetic field can produce scattered radiation at the cyclotron harmonics.

Given the spectrum of electron and ion fluctuations, the calculation of the scattering is straightforward but too long to record here. Only the results will be given. We shall take the externally imposed magnetic field to lie along the z axis with an electron cyclotron frequency ω_c. We shall assume that the spectrum of (random) longitudinal electron waves (fluctuations) has a magnitude that generally is greater than the equilibrium level. The ions are assumed to have infinite mass, but to be correlated with each other. The average electron and ion densities are n_e and n_i, respectively. The fluctuations of

electron and ion density are denoted $n_e \delta\rho_e(\vec{r}, t)$ and $n_i \delta\rho_i(\vec{r})$. The spectral density of electron fluctuations, $\left\langle \delta\rho_e \delta\rho_e \middle| \vec{K},\omega \right\rangle$, is defined as

$$\left\langle \delta\rho_e \delta\rho_e \middle| \vec{K},\omega \right\rangle = \int_{-\infty}^{\infty} d\tau\, e^{-i\omega\tau} \int d\vec{a}\, e^{-i\vec{K}\cdot\vec{a}} \left\langle \delta\rho_e(\vec{r}, t)\, \delta\rho_e(\vec{r}+\vec{a}, t+\tau) \right\rangle.$$

Here, the angular brackets denote an ensemble average. In similar fashion, we define the spectral density of ion fluctuations as

$$\left\langle \delta\rho_i \delta\rho_i \middle| \vec{K} \right\rangle = \int d\vec{a}\, e^{-i\vec{K}\cdot\vec{a}} \left\langle \delta\rho_i(\vec{r})\, \delta\rho_i(\vec{r}+\vec{a}) \right\rangle.$$

The electron fluctuations will be scattered by the ion fluctuations, and produce longitudinal and transverse current-density fluctuations whose spectral density $\left\langle \delta\vec{j}\, \delta\vec{j} \middle| \vec{k},\omega \right\rangle$ is given (approximately) by

$$\left\langle \delta\vec{j}_r \delta\vec{j}_s \middle| \vec{k},\omega \right\rangle = \int d\vec{K}\, g_{rs} \left| b(\vec{K},\omega) \right|^2 \left\langle \delta\rho_e \delta\rho_e \middle| \vec{K},\omega \right\rangle \left\langle \delta\rho_i \delta\rho_i \middle| -\vec{K} \right\rangle,$$

where

$$g_{xx} = K_\perp^2 \frac{\omega^2 + \omega_c^2}{\left(\omega^2 - \omega_c^2\right)^2}$$

$$g_{zz} = K_z^2 \frac{1}{\omega^2}$$

$$g_{xz} = 0$$

$$b(\vec{K}, \omega) = K^{-4} \sum_{m=-\infty}^{+\infty} m\omega_c \omega_p^4 n_e e \int d\vec{v} \frac{J_m^2\left(\frac{K_\perp v_\perp}{\omega_c}\right) \frac{\partial}{\partial v^2} f_e(v^2)}{\omega + K_z v_z + m\omega_c - i\epsilon}.$$

Here, ω_p is the electron plasma frequency, J_m is a Bessel function, and $K_\perp^2 = K_x^2 + K_y^2$.

The emission power density of scattered radiation into the mode $(\vec{k}, \omega)$ is proportional to $\left\langle \delta\vec{j}\delta\vec{j} \middle| \vec{k},\omega \right\rangle$. The actual flux reaching a receiver outside the plasma depends, of course, on the dielectric properties of the plasma, including the reflection at the boundaries. One may expect (at least for an optically thin plasma) that the gross features of the spectrum of $\left\langle \delta\vec{j}\delta\vec{j} \middle| \vec{k},\omega \right\rangle$ will be present in the observed spectrum.

For convenience, we shall take $\left\langle \delta\rho_i \delta\rho_i \middle| \vec{K} \right\rangle$ to be the familiar equilibrium expression

$$n_i^{-1} \frac{K^2 + \frac{1}{2}\lambda_D^{-2}}{K^2 + \lambda_D^{-2}}.$$

If $K_z \ll \lambda_D^{-1}$ and $K_\perp \approx \lambda_D^{-1}$, then $|b(\vec{K},\omega)|^2$ has maxima at $\omega = m\omega_c$. Now suppose that when $K_\perp \approx \lambda_D^{-1}$, $\langle \delta\rho_e \delta\rho_e | \vec{K},\omega \rangle$ is large only for $K_z \ll \lambda_D^{-1}$. Then $\langle \delta\vec{j}\delta\vec{j} | \vec{k},\omega \rangle$ will also have the observed maxima at the cyclotron harmonics. Furthermore, this choice of the electron fluctuation spectrum is not entirely artificial. One might expect just such a spectrum in situations in which the unstable modes are those that travel in a direction approximately perpendicular to the magnetic field so that the Landau damping is at a minimum.

Since $\langle \delta\rho_e \delta\rho_e | \vec{K},\omega \rangle$ should not be large for $\omega > \omega_p$, one would not expect to observe harmonics at frequency greater than ω_p. This prediction is in agreement with experiments.

T. H. Dupree

References

1. G. Bekefi, J. D. Coccoli, E. B. Hooper, Jr., and S. J. Buchsbaum, Phys. Rev. Letters 9, 6 (1962).

2. A. Simon and M. N. Rosenbluth (paper to be published in Phys. Fluids).

I. ERRATA: SCATTERING OF LIGHT FROM (PLASMA) ELECTRONS II

In a report with this title, published in Quarterly Progress Report No. 69 (pages 74-79), corrections should be made in two equations.

Page 76 – the third and fourth equations from the top of the page should read:

$$V^* = \frac{\Delta\lambda_2}{\lambda_o} c \frac{1}{1 + \cos\theta}.$$

Hence

$$dN_{V_a} = \frac{N}{\sqrt{2\pi}} \left(\frac{m}{2kT_e}\right)^{1/2} \frac{c}{\lambda_o} (1+\cos\theta)^{-1/2} \exp\left(- \frac{mc^2(1+\cos\theta)^{-1}}{4k\lambda_o^2} \frac{\Delta\lambda_2^2}{T_e} \right) d\lambda,$$

E. Thompson, G. Fiocco

J. CONCENTRATION OF EXCITED STATES IN A LOW-ENERGY CESIUM PLASMA

1. Introduction

In a low-energy cesium plasma ions are lost continuously by ambipolar diffusion and recombination. In the absence of a sufficient external ion source these losses have to be balanced by ionization processes occurring in the plasma. Ionization occurs mainly by inelastic collisions between electrons and cesium atoms. With electrons of low energy most of these collisions lead to the first excited state of the cesium atom, that is, the normal 6s level of the valence electron is excited to the 6p level. Ionization can then occur by further collisions of these excited atoms. In this report the concentration of atoms in the first excited state is calculated as a first step toward obtaining the rates of ionization from excited states.

The concentration of excited states is mainly determined by excitation and de-excitation collisions with electrons and by emission and absorption of resonance radiation. The results of calculations on the required electron collision cross sections are given in this report. The problem of radiation trapping, that is, the successive emission and absorption of resonance radiation, is also treated. An over-all rate balance is used to determine the concentration of excited states.

The calculations are carried out for a cesium density of 2×10^{16} cm^{-3}, a cesium temperature of 1000°K, an electron density of 10^{14} cm^{-3}, electron temperature of approximately 3000°K, and a plasma thickness of 0.025 cm. These values are typical for the high-current mode of a cesium thermionic-energy converter and can be varied considerably without affecting the conclusions.

2. Electron Cross Sections

The cross-section curve for excitation of cesium atoms to the first excited state by electron collisions has not been measured. The excitation curve has been measured, however, and calculated theoretically for sodium, which is very similar to cesium in its atomic properties. Because of this similarity, the same theoretical method that yielded good agreement with the experimental data for sodium is used to calculate the inelastic cross-section curve for cesium.

The total electron collision cross section represents an upper limit to the inelastic cross section. Total cross-section curves were measured by Brode[1] for the alkali metals – sodium, potassium, rubidium, and cesium. All of the curves have similar shapes, showing a peak at electron energies of approximately 2 ev and decreasing at higher energies. The curve for cesium shows the highest cross sections, with a peak value of 570×10^{-16} cm^2. This leads to the expectation that the inelastic electron cross sections for cesium will also be large and will be similar to, but somewhat higher than,

those for the other alkali metals.

The general shape of the electron cross-section curve for excitation from the ground state is well known. The cross section is zero up to the excitation potential; then it rises sharply with increasing electron energy, levels off to a peak a few volts above the excitation potential, and then declines. Such curves have been measured for sodium, helium, and mercury.[2]

In this report we are interested mainly in the initial rise of the excitation curve because there are very few electrons in the plasma with energies higher than a few ev. In the low-energy region the normal Born approximation yields cross sections that are too large. Recently, Seaton[3] has developed a semi-classical "impact-parameter" method for calculating electron excitation cross sections of optically allowed transitions. This method yields results that are in good agreement with a variety of available experimental data at low electron energies. To see this point clearly, let us consider the case of the excitation of sodium to the first excited state, that is, the 3s-3p transition.

In the impact-parameter method the motion of the colliding electron is taken to be rectilinear. The cross section is calculated in terms of the contributions from different impact parameters R, where R is the classical distance of closest approach. With initial state i and impact parameter R_i, let there be a probability $P_{ji}(R_i)$ that the $i \rightarrow j$ transition occurs. The cross section is

$$\sigma(i \rightarrow j) = \int_0^\infty P_{ji}(R_i)\, 2\pi R_i\, dR_i. \tag{1}$$

The probability of transition P_{ji} is calculated from time-dependent perturbation theory, under the assumption that the atomic potential follows the simple Coulomb law. This assumption is valid for $R_i \gg r_a$, where r_a is a length that is comparable with the atomic dimensions, but it is invalid for $R_i \leq r_a$. For some transitions with large cross sections such as the 3s-3p transition in sodium the calculated values of P_{ji} violate the conservation condition, $P_{ji} \leq 1$, for the smaller impact parameters. For these transitions the impact-parameter method introduces a cutoff in Eq. 1 at an impact parameter R_1 which is such that

$$P_{ji}(R_1) = 1/2. \tag{2}$$

For $R_i < R_1$ the probability P_{ji} is considered as an oscillatory function with a mean value of 1/2. The cross section then is

$$\sigma(i \rightarrow j) = \frac{1}{2}\pi R_1^2 + \int_{R_1}^\infty P_{ij}(R_i)\, 2\pi R_i\, dR_i. \tag{3}$$

Seaton[3] used the impact-parameter method to calculate the inelastic scattering cross

section for excitation to the first excited state of the sodium atom, that is, for the 3s-3p transition. These calculations were repeated and resulted in the cross-section curve shown in Fig. XII-31. This figure also shows absolute cross-section measurements by Christoph[4] as corrected by Bates,[2] and relative cross-section measurements by Haft[5] as reported by Christoph,[4] scaled to agree with the absolute measurements. Haft's data as reported here differ somewhat from the curve drawn by Bates,[2] who does not seem to consider Haft's low-energy points and scaled the data to agree with Christoph's absolute measurements at high electron energies, for which Haft's values are too high because of Doppler broadening of the spectral lines that he observed.

As shown in Fig. XII-31, the impact-parameter approximation gives very good agreement with the experimental data down to 0.8 ev above the excitation potential, which is 2.1 ev for sodium. At these very low energies, Haft's data are not very accurate, but the agreement is actually better than shown, since in Haft's experiment the electron energies had a spread of approximately 0.4 ev below their nominal value. At the excitation potential, the impact approximation curve is clearly in error, since it does not go to zero there. The Born approximation curve is much too high at low energies.

The good agreement between theory and experiment for the 3s-3p excitation of sodium encouraged the application of the theory to a very similar case, the 6s-6p excitation of cesium. The two 6p levels of cesium lie close together approximately 1.4 ev above the ground state. As for sodium, the two levels were treated together and yielded the excitation cross-section curve shown in Fig. XII-32. The curve is very similar to that for sodium; the maximum is higher and occurs at a lower energy, as expected in view of the

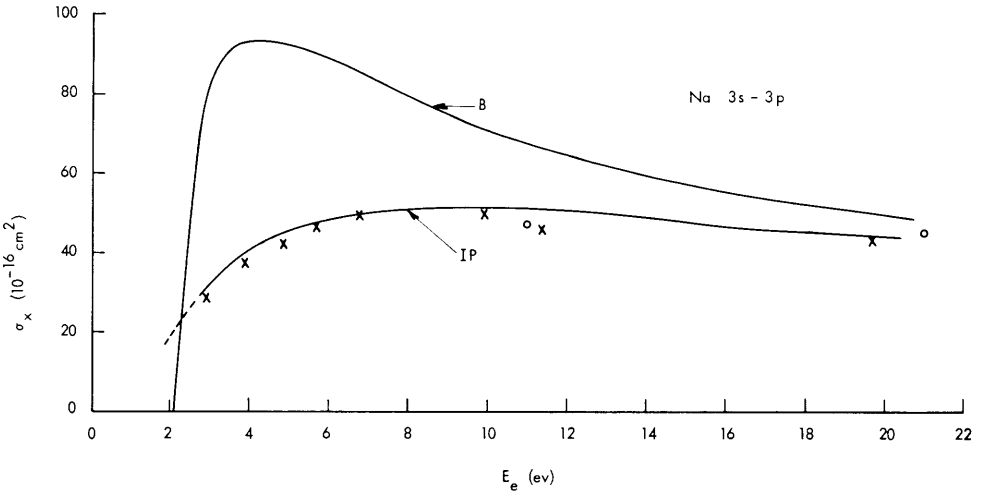

Fig. XII-31. The 3s-3p inelastic electron collision cross section of sodium as a function of electron energy. B, Born approximation; IP, impact-parameter approximation; O, experimental (Christoph, absolute); x, experimental (Haft, relative).

larger total collision cross section and lower excitation energy of cesium. Judged from the data for sodium, the curve for cesium should be correct down to electron energies of 2.2 ev. For lower electron energies a conservatively low estimate of the dependence of the excitation cross section on electron energy E is

$$\sigma_x(E) = 75 \times 10^{-16}(E-1.4)\ \text{cm}^2$$
$$1.4 \leq E \leq 2.2\ \text{ev}. \tag{4}$$

Once the excitation cross section is known, the de-excitation cross section can be calculated by invoking the principle of detailed balance. According to this principle, the rates of electron excitation and de-excitation must be equal under thermal equilibrium at all temperatures. It has been shown directly by Fowler[6] that the relation between the de-excitation cross section σ_d and the excitation cross section σ_x is given by

$$\frac{\sigma_d(E)}{\sigma_x(E+E_x)} = \frac{\omega_o}{\omega_x}\frac{E+E_x}{E}, \tag{5}$$

where E_x is the excitation potential and ω_o and ω_x are the statistical weights of the ground state and the excited state. The de-excitation cross section for cesium 6p-6s has been calculated and is shown in Fig. XII-32. It is approximately constant in the energy range plotted.

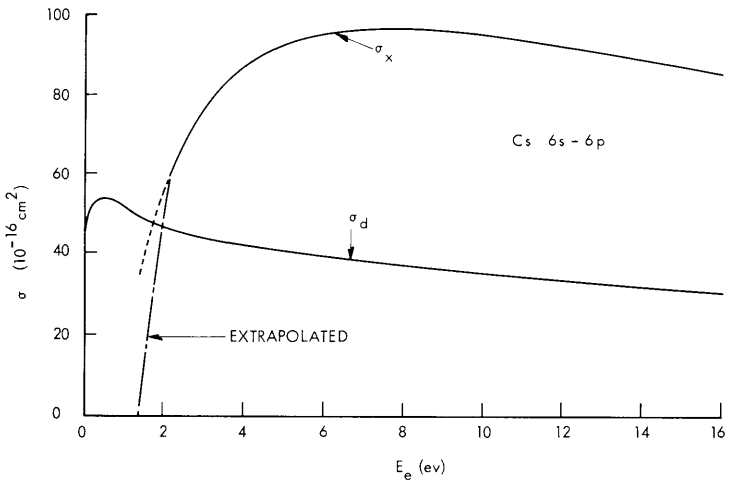

Fig. XII-32. The 6s-6p excitation and de-excitation electron collision cross section of cesium as a function of electron energy. Impact-parameter approximation.

3. Radiation Trapping

One source of losses of excited atoms in a cesium plasma is the spontaneous emission of resonance radiation. This radiation consists of sharp lines that have a high probability of absorption by atoms in the ground state. The process of successive absorption and emission of resonance radiation, called "radiation trapping," results in an effective lifetime that is larger than the natural lifetime of the excited state.

The total rate of decay of excited states by spontaneous emission is n_x/τ_n cm^{-3} sec^{-1}, where n_x is the concentration, and τ_n the natural lifetime of the excited state. Suppose that the emitted radiation has an average probability p of escaping from the plasma without absorption. Then the rate at which these photons leave the plasma is

$$\nu_r = \frac{n_x p}{\tau_n} \text{ cm}^{-3} \text{ sec}^{-1}. \tag{6}$$

This is equal to the net radiation loss of excited states per unit volume. Equation 6 can be written

$$\nu_r = n_x/\tau_{eff}, \qquad \tau_{eff} = \tau_n/p, \tag{7}$$

where τ_{eff} is the effective lifetime for radiative decay of the excited state, averaged over the plasma. If the photon-escape probability p is small, then τ_{eff} will be much larger than τ_n. In this report we are concerned only with low radiation densities, where radiation-stimulated emission is not important.

An expression for the average radiation-escape probability will be derived from the absorption cross section and the emission line shape, for a cesium plasma between two semi-infinite flat plates. Any radiation reaching the plates will be considered to be lost. It will be seen that the calculations can be easily extended to other resonance lines if certain physical data are available.

a. Photon Absorption Cross Section and Emission Probability

In calculating the average radiation-escape probability p we must consider the detailed shape of the emitted line and of the corresponding absorption cross section. Several disturbing influences cause these shapes to differ from a pure delta function; these influences are said to broaden the lines. Under thermodynamic equilibrium the shapes of the absorption and emission lines are the same, since detailed balancing between emission and absorption must hold at all frequencies. This means that the effect of a broadening mechanism must only be known well for either absorption or emission in order to calculate the photon-escape probability.

In the plasma under consideration the dominant broadening mechanism is pressure broadening. It is due to collisions between excited states and ground-level atoms of the

same species that cause broadening, frequency shift, and asymmetry of the absorption cross section.[7] The escape probability of photons is determined by the line shape in the wings of the line, far from the center. In this region the absorption shape follows closely the simple Breit-Wigner formula:

$$\sigma_\nu = \sigma_o \frac{(\Gamma_p/2)^2}{(\Gamma_p/2)^2 + (\nu-\nu_o)^2}. \tag{8}$$

Here, ν is the radiation frequency, σ_o is the absorption cross section at the resonance frequency ν_o, and Γ_p is the halfwidth (full width at half-maximum) resulting from pressure broadening. The absorption cross section at the edges of the resonance curve of the cesium 6s-6p transition has been measured by Gregory.[8] His data agree well with the theoretical result of Furssow and Wlassow,[9] who calculated the halfwidth resulting from pressure broadening to be

$$\Gamma_p = \frac{2}{3\pi} \frac{e^2}{m_e \nu_o} n_o f, \tag{9}$$

where n_o is the density of atoms in the ground state and f is the oscillator strength for the transition.

The value of σ_o can be obtained from a consideration of thermodynamic equilibrium between the radiation and the atoms. The derivation has been given by several authors.[10,11] It can be shown that the integral of the absorption cross section over the resonance is proportional to the oscillator strength, f:

$$\int \sigma_\nu \, d\nu = \frac{\pi e^2}{m_e c} f. \tag{10}$$

Combining Eqs. 8-10 yields

$$\sigma_\nu = \frac{3\pi}{n_o \lambda_o} \frac{1}{1 + t^2}, \tag{11}$$

where λ_o is the wavelength at the resonance frequency ν_o and

$$t = \frac{\nu - \nu_o}{\Gamma_p/2}. \tag{12}$$

The emission probability $p(\nu)$ is just the Breit-Wigner shape scaled to give a total emission probability of unity:

$$p(\nu) = \frac{1}{\pi} \frac{\Gamma_p/2}{(\Gamma_p/2)^2 + (\nu-\nu_o)^2}. \tag{13}$$

b. Calculation of the Photon Escape Probability

Consider a semi-infinite plasma of dimension s, as shown in Fig. XII-33.

Suppose that an excited atom at position x decays by emitting a photon of frequency ν in the direction r. The excape probability for this photon is $\exp(-n_o\sigma_\nu r)$. To obtain the average excape probability over the emission spectrum one must multiply this exponential

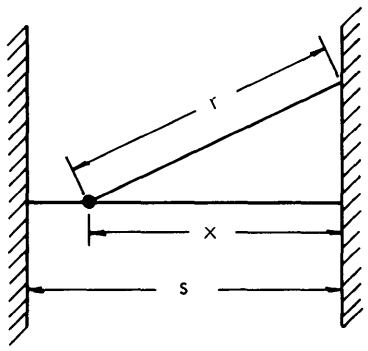

Fig. XII-33. Schematic diagram of the plasma geometry.

factor by the emission probability $p(\nu)$ and integrate over all frequencies. Similarly, the average over all directions of emission is obtained by multiplying by p(r), the probability of emission in a direction between r and r + dr, and by integrating over all r. Finally, this is averaged over all values of x. The average escape probability then is given by

$$p = \frac{1}{s}\int_0^s dx \int_x^\infty p(r)\, dr \int_0^\infty p(\nu)\, e^{-n_o\sigma_\nu r}\, d\nu. \tag{14}$$

The photons are emitted with equal probability in all directions. The directional emission probability is

$$p(r) = \frac{x}{r^2} \qquad \int_x^\infty p(r)\, dr = 1. \tag{15}$$

Combining Eqs. 11-15 yields

$$p = \frac{1}{\pi s}\int_0^s x\, dx \int_x^\infty \frac{dr}{r^2} \int_{-\infty}^\infty \frac{dt}{1+t^2} \exp\left(-3\pi \frac{r}{\lambda_o}\frac{1}{1+t^2}\right). \tag{16}$$

This integral is rather difficult to evaluate. A first approximation can easily be obtained, since only photons with frequencies far out in the wings contribute significantly to the average escape probability. For these photons $t^2 \gg 1$. If we neglect 1 in comparison with t^2 in Eq. 16 the integral is readily evaluated to be

$$p = \frac{4}{3\pi}\sqrt{\frac{\lambda_o}{3s}}. \tag{17}$$

A second approximation to the integral in Eq. 16 was obtained by separating it into two integrals: one for low values of r, and one for high values. The result is

$$p = \frac{4}{3\pi}\sqrt{\frac{\lambda_o}{3s}}\left(1 - \frac{1}{11}\sqrt{\frac{\lambda_o}{s}}\right). \tag{18}$$

Since $\lambda_o \ll s$, the correction introduced is negligible and the first approximation, Eq. 17, gives the average escape probability with sufficient accuracy. This result shows that we were justified in ignoring the detailed shape of the line near the center, since this region contributes very little to the escape probability.

c. Calculation of the Effective Lifetime of the Excited States

Equations 7 and 17 give the effective lifetime as

$$\tau_{eff} = \tau_n \frac{3\pi}{4}\sqrt{\frac{3s}{\lambda_o}}. \tag{19}$$

For the cesium 6p state, $\tau_n = 3.5 \times 10^{-8}$ sec, and $\lambda_o = 0.87 \times 10^{-4}$ cm. With a plasma spacing, s, of 0.025 cm, the effective lifetime is

$$\tau_{eff} = 2.4 \times 10^{-6} \text{ sec}. \tag{20}$$

It is interesting to note that the effective lifetime is independent of the cesium atom density. This is only true as long as cesium atoms are the dominant source of resonance line broadening.

4. Rate Balances

The concentration of excited states is primarily determined by the rate of excitation ν_x ($\text{cm}^{-3}\ \text{sec}^{-1}$), the rate of de-excitation ν_d, and the net rate of radiative decay ν_r. The last rate is determined by the effective lifetime τ_{eff} of the excited states. The rate balance is

$$\nu_x = \nu_d + \nu_r. \tag{21}$$

The rate of de-excitation is

$$\nu_d = n_x n_e \int_0^\infty f_e(E)\, \sigma_d(E)\, v_e(E)\, dE, \tag{22}$$

where $f_e(E)$ is the electron energy distribution function, and n_e and v_e are the electron

density and velocity. Since σ_d is approximately constant in the low-energy range of interest, Eq. 22 can be written

$$\nu_d = n_x n_e \bar{\sigma}_d \bar{v}_e.$$

Combining this with Eqs. 7 and 21 yields

$$\frac{\nu_x - \nu_d}{\nu_d} = \frac{1}{\tau_{eff} n_e \bar{\sigma}_d \bar{v}_e} \equiv R, \tag{23}$$

where $\bar{\sigma}_d = 50 \times 10^{-16}$ cm^2, $\bar{v}_e = 3 \times 10^7$ cm/sec, $\tau_{eff} = 2.4 \times 10^{-6}$ sec, and $n_e = 10^{14}$ cm^{-3}. With these values, Eq. 23 becomes

$$\frac{\nu_x - \nu_d}{\nu_d} = R = 0.028. \tag{24}$$

Since $R \ll 1$, the density of the first excited state is essentially determined by electron collisions. The rate of excitation is

$$\nu_x = n_o n_e \int_{E_x}^{\infty} f_e(E)\, \sigma_x(E)\, v_e(E)\, dE. \tag{25}$$

It is now necessary to specify the electron energy distribution. If this distribution is Maxwellian, then the integrals in Eqs. 22 and 25 are unique functions of the electron temperature T_e. Taking the ratio of the two equations yields

$$\frac{\nu_d}{\nu_x} = \frac{n_x}{n_o} F(T_e). \tag{26}$$

The function $F(T_e)$ can be determined, since at equilibrium $\nu_x = \nu_d$ and

$$\left(\frac{n_x}{n_o}\right)_{equil} = \frac{\omega_x}{\omega_o} \exp\left(-\frac{E_x}{kT_e}\right), \tag{27}$$

so that

$$\frac{\nu_d}{\nu_x} = \frac{n_x}{n_o}\frac{\omega_o}{\omega_x} \exp\left(\frac{E_x}{kT_e}\right). \tag{28}$$

Combining Eqs. 23 and 28 yields

$$\frac{n_x}{n_o} = \frac{\omega_x}{\omega_o} \exp\left(-\frac{E_x}{kT_e}\right)\frac{1}{1+R}. \tag{29}$$

Since R « 1, the density ratio of excited to ground states is close to the equilibrium value given by Eq. 27. This ratio is plotted in Fig. XII-34.

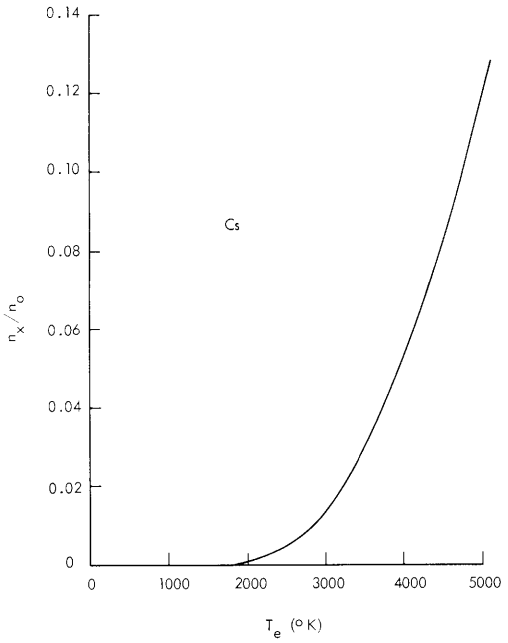

Fig. XII-34. Equilibrium density ratio of the 6p excited state and ground state of cesium plotted as a function of electron temperature.

There is a large number of other mechanisms that affect the density of excited states in a plasma, and it is virtually impossible to calculate the contribution of each of them. It has been shown in this report, however, that the inelastic electron collision cross sections are very large. Since the electron density is quite high, the inelastic electron collision rates are dominant in determining the concentration of the first excited state. This conclusion is directly applicable to the plasma in the high-current mode of a cesium thermionic-energy converter.

H. L. Witting

References

1. R. B. Brode, The absorption coefficient for slow electrons in alkali metal vapors, Phys. Rev. 34, 673 (1929).

2. D. R. Bates, A. Fundaminsky, H. S. W. Massey, and J. W. Leech, Excitation and ionization of atoms by electron impact – the Born and Oppenheimer approximations, Phil. Trans. Roy. Soc. London A243, 93 (1950).

3. M. J. Seaton, The impact parameter method for electron excitation of optically allowed atomic transitions, Proc. Phys. Soc. (London) 79, 1105 (1962).

4. W. Christoph, Ann. Phys. 23, 51 (1935).

5. G. Haft, Z. Phys. 83, 73 (1933).

6. R. H. Fowler, Phil. Mag. 47, 257 (1924).

7. A. C. G. Mitchell and M. W. Zemansky, Resonance Radiation and Excited Atoms (Cambridge University Press, London, 1961).

8. C. Gregory, Phys. Rev. 61, 465 (1942).

9. W. Furssow and A. Wlassow, Physik. Z. Sowjetunion 10, 378 (1936).

10. R. W. Nichols and A. L. Stewart, Allowed transitions, Atomic and Molecular Processes, edited by D. R. Bates (Academic Press, Inc., New York, 1962), Chapter 2, p. 49.

11. A. C. G. Mitchell and M. W. Zemansky, op. cit., p. 96.

K. ELECTRON GUN FOR PRODUCTION OF A LOW-DIVERGENCE BEAM

A program has been initiated to determine experimentally the properties of the corkscrew.[1] An electron beam of low current (0.1-20 μa) and minimum divergence (less than

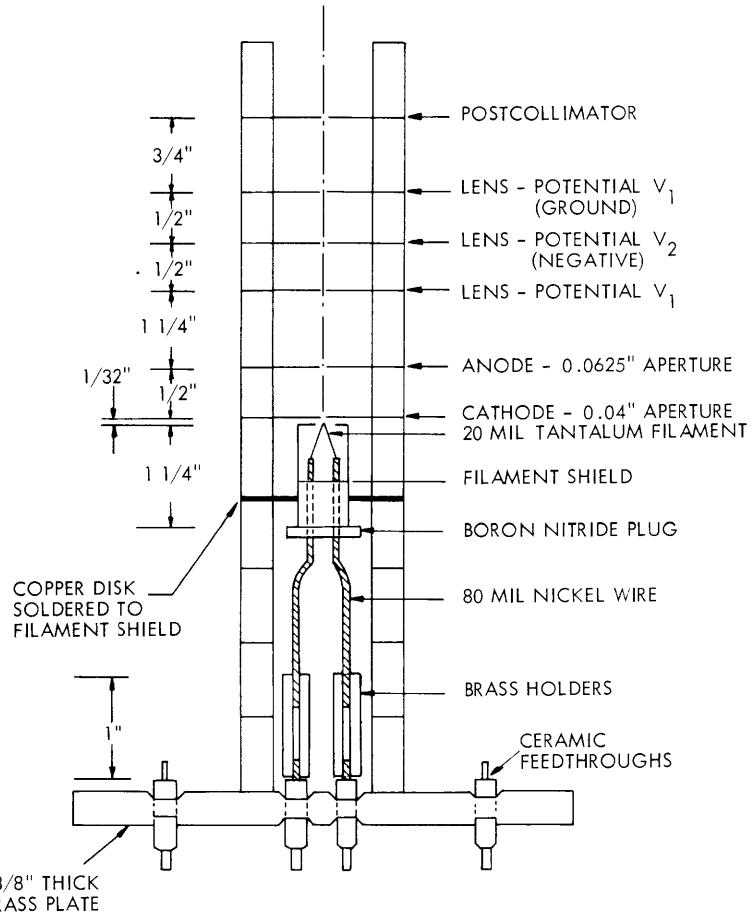

Fig. XII-35. Electron gun for the production of a low-divergence beam.

1/500 radian) will be required, and an electron gun has been constructed to produce the beam. The properties of the present model are:

Beam Current, 0.1-5 μa

Gun Length, 20 cm

Lens Aperture, 0.159-cm diameter

Cathode Aperture, 0.102-cm diameter.

The electron gun is shown in Fig. XII-35.

The beam currents investigated (0.1-3 μa) were well within the region of negligible space-charge effects, thereby giving a divergence angle of 1/1000 radian at a distance of 2000 lens aperture radii from the end of the gun for a beam current of approximately 15 μa.

In three separate trials, the average beam-divergence angles over the path length investigated (1.5 meters) were 1.8, 1.91, and 1.59×10^{-3} radian.

The observed divergences can be attributed to aberration effects in the gun; spherical aberration is the predominant cause. Alterations that will be applied to reduce the aberrations are: (a) adjustment of one relative aperture of one negative lens element, and (b) addition of postcollimators to define the beam and remove widely divergent particles.

The gun will then be scaled down by a factor of approximately four for insertion in the corkscrew experiment.

P. Karvellas

References

1. D. J. Rose, R. C. Wingerson, and S. J. Tulenko, Helical resonant beam trapping, Quarterly Progress Report No. 63, Research Laboratory of Electronics, M.I.T., October 15, 1961, pp. 41-44.

L. SPACE-CHARGE NEUTRALIZATION EXPERIMENT

The purpose of the experiment is to examine ways of injecting electrons into an ion beam in order to neutralize its space charge and avoid the consequent stalling of the beam. Practical applications of the experiment arise in spacecraft ion propulsion.

The ion beam is extracted from a cesium ion source which is shown schematically in Fig. XII-36.

The porous tungsten ionizer, a, through which the cesium atoms diffuse, is heated to approximately 1200°C by electron bombardment of its tantalum support.

The method by which electrons are brought into the region of the ion beam is by extracting them from a filament, c, through the accelerating grid, b.

The experiments were performed in a 14 in. × 15 in. × 36 in. aluminum vacuum

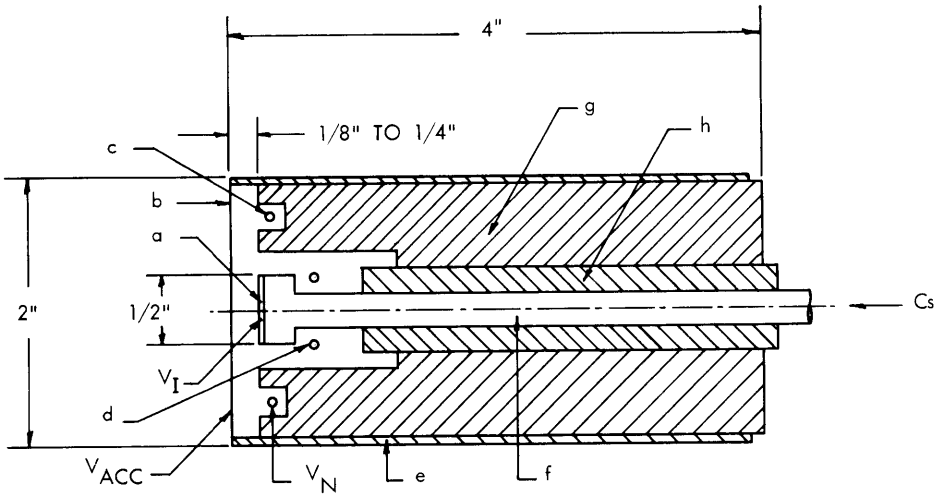

Fig. XII-36. Cesium ion source.
a. Porous tungsten ionizer
b. Accelerating grid
c. Filament producing neutralizing electrons
d. Filament for heating the ionizer
e. Accelerating electrode
f. Tantalum tube for Cs supply
g. Insulator
h. Insulator

chamber, under a pressure of approximately 2×10^{-6} mm Hg.

The current, I, was measured on a collector, 8 inches in diameter, placed 30 inches away from the source. The collector, as well as the vacuum chamber, was at ground potential. The voltage of the ionizer, the accelerating grid, and the neutralizing filament will be denoted V_I, V_{Acc}, and V_N, respectively.

Under steady-state operation of the source, currents I of from 10 ma to 20 ma at voltages, V_I, of 3000-5000 volts were obtained, without any neutralizing electrons being introduced. Space-charge considerations show that an unneutralized ion beam for such currents is impossible at these voltages. Therefore one must conclude that electrons were obtained from the environs (for example, by secondary emission from the walls). The electrons are trapped in the volume of the beam (for example, by losing energy through inelastic collisions), and in this way form a neutral path through which the ion current can pass.

This type of neutralization will not occur in space, of course. Its presence, though, in the laboratory does not allow testing of other ways of injecting electrons.

In order to overcome this difficulty, we examined the time period immediately after the ion extraction voltage is applied and before the described volume neutralization is completed.

The ionizer voltage V_I was applied as a step with a rise time of less than 0.5 μsec,

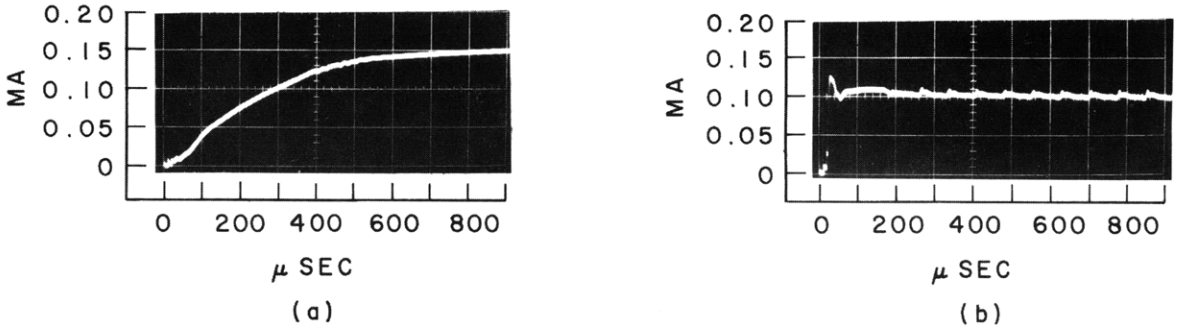

Fig. XII-37. Collected ion currents.
V_I = 600 volts, V_{Acc} = 100 volts, V_N = 0. Transit time, 22 μsec.
(a) No electrons: rise time, ~500 μsec.
(b) With electrons: rise time, ~25 μsec.

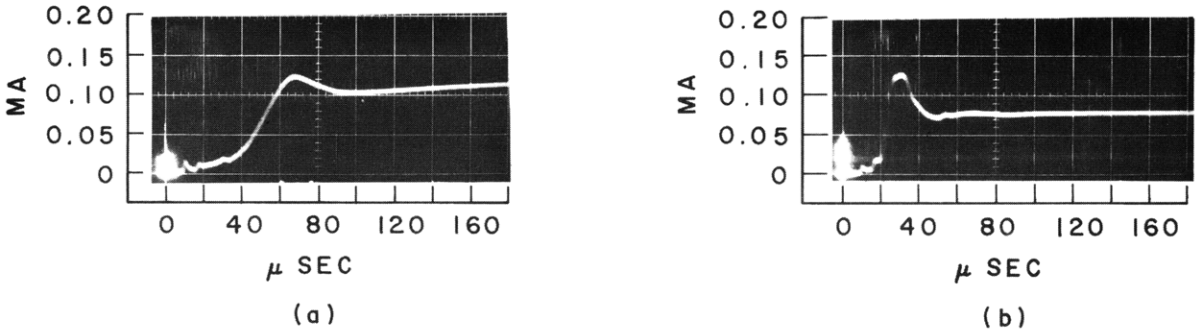

Fig. XII-38. Collected ion currents.
V_I = 1000 volts, V_{Acc} = 200 volts, V_N = 100 volts.
Transit time, 18 μsec.
(a) No electrons: rise time, ~60 μsec.
(b) With electrons: rise time, ~20 μsec.

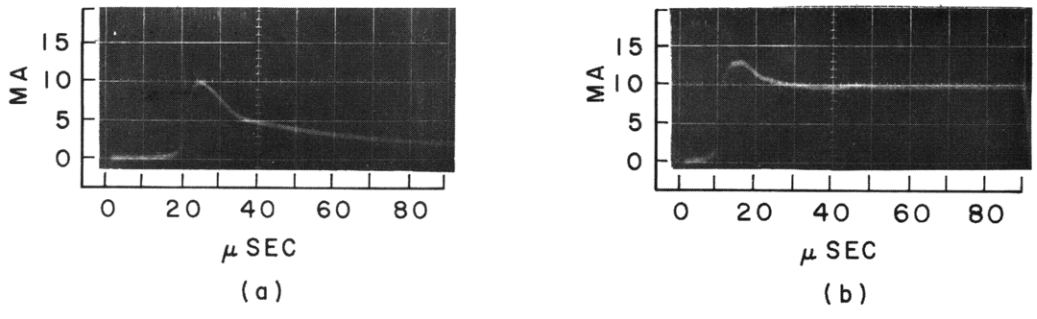

Fig. XII-39. Collected ion currents.
V_I = 4000 volts, V_{Acc} = 300 volts, V_N = 100 volts.
Transit time, 9 μsec.
(a) No electrons: rise time, ~20 μsec.
(b) With electrons: rise time, ~10 μsec.

and the collector current I was subsequently recorded on an oscilloscope.

At low voltages ($V_I < 700$ volts) we found that the time taken for the full ion current to reach the collector was considerably longer than the transit time for ions of this energy (Fig. XII-37a). This fact indicates that the beam is temporarily stopped by its excessive space charge until enough electrons are accumulated from the environs and trapped in the beam to achieve neutralization.

When electrons were injected from the neutralizing filament the current on the collector reached its full value in a time that was close to the ion transit time.

For example, at $V_I = 600$ volts and $I \approx 0.1$ ma (Fig. XII-37), the full current reaches the collector in approximately 500 μsec without electrons, and in approximately 25 μsec with electrons. The ion transit time is 22 μsec.

Similar results have been reported by Sellen and Kemp[1] when electrons are made available to the beam from hot filaments placed in its proximity.

At higher extraction voltages and ion currents, the time taken for the beam to reach the collector when no electrons are introduced is much shorter, being only 2 or 3 times the transit time. It appears that under these conditions electrons can be obtained and trapped faster than before, probably because of the higher electric fields that are present.

Introduction of electrons reduces this time still further, bringing it to the level of the transit time. For example, at $V_I = 1000$ volts, $I = 0.1$ ma (Fig. XII-38), introduction of electrons reduces the rise time from approximately 60 μsec to approximately 20 μsec, against a transit time of 18 μsec.

At $V_I = 4000$ volts, $I = 10$ ma (Fig. XII-39) the rise time is approximately 20 μsec without electrons and approximately 10 μsec with electrons, while the transit time is 9 μsec.

These results indicate that electrons introduced in the region of the beam by an electron gun are effective in neutralizing the beam space charge.

Further experiments are in progress in order to establish the exact beam pattern under various conditions. To accomplish this, the walls of the chamber have been covered with isolated metallic strips, and the collected currents individually measured.

The effect of variations in different parameters, such as the accelerating grid voltage V_{Acc}, neutralizer voltage V_N, etc., on the behavior of the beam, is also being investigated.

G. C. Theodoridis

References

1. J. M. Sellen and R. F. Kemp, Cesium Ion Beam Neutralization in Vehicular Simulation, American Rocket Society Paper 61-84-1778, presented at the IAS-ARS Joint Meeting, Los Angeles, California, June 1961.